A large, faint red circular graphic composed of many small, overlapping triangles, resembling a stylized ring or a thick line, positioned in the upper right quadrant of the page.

Masterarbeit im Studiengang Physik

Laser Control of Topological Polaritons

Damian Hofmann

27. November 2018

Fachbereich Physik
Fakultät für Mathematik, Informatik und Naturwissenschaften
Universität Hamburg

Angefertigt am

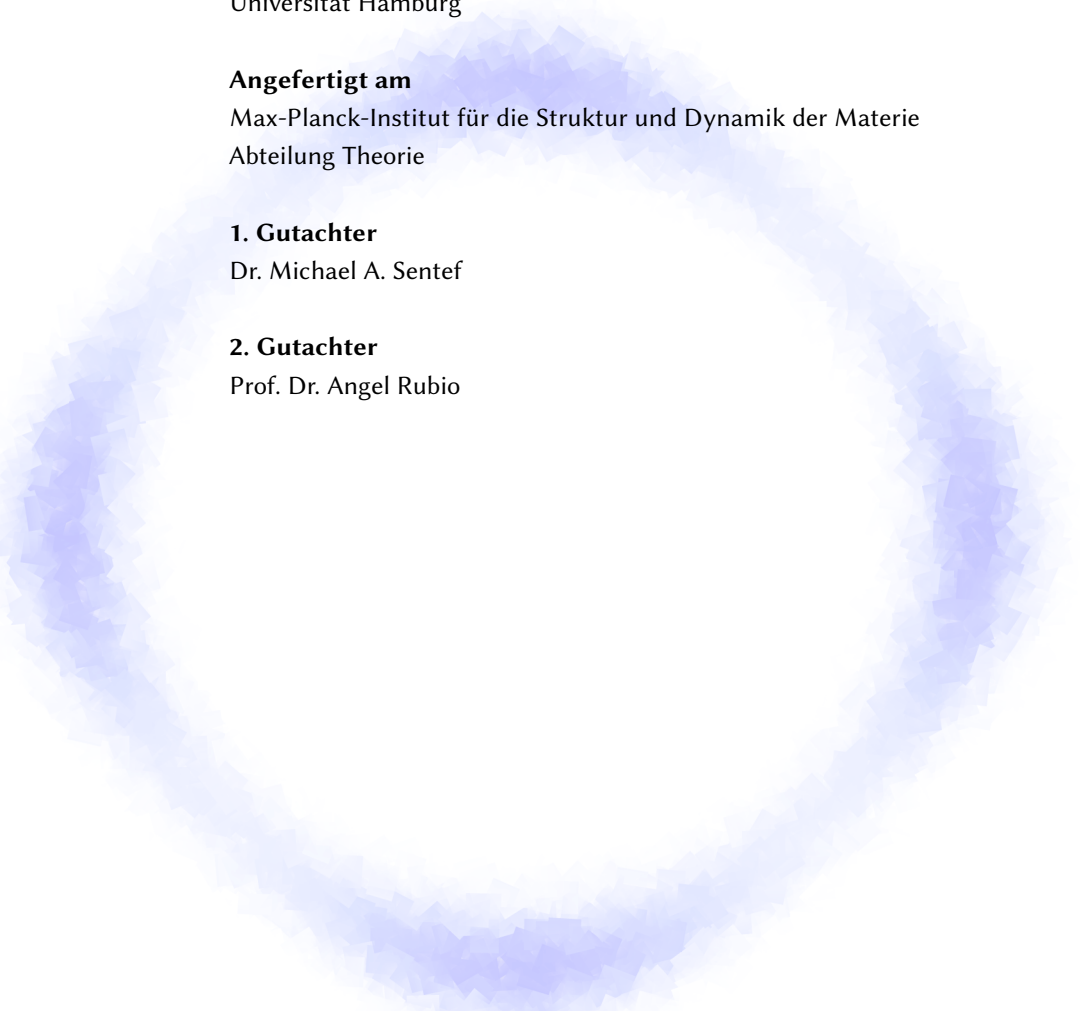
Max-Planck-Institut für die Struktur und Dynamik der Materie
Abteilung Theorie

1. Gutachter

Dr. Michael A. Sentef

2. Gutachter

Prof. Dr. Angel Rubio

A large, faint blue circular graphic composed of many small, overlapping triangles, resembling a stylized ring or a thick line, positioned in the lower left quadrant of the page.

Abstract

Polaritons are quasi-particles consisting of a superposition of photons and excitons, which can be created inside semiconductor quantum wells in optical cavities. In this master thesis, we study a system in which multiple semiconductor layers are coupled through a single photonic cavity mode. A momentum-dependent complex phase in the coupling of the excitons to the light field gives rise to intrinsic non-trivial topological properties of the polariton bands. In particular, the system possesses chiral edge modes, which can be excited by optical pumping near the sample boundary. We simulate the dynamics of the driven system in the semi-classical approximation using a dissipative Gross-Pitaevskii equation, which allows us to study topologically protected chiral transport along the edges of a finite sample. We further discuss the dynamics of a lattice version of the topological polariton model, from which we can obtain time-resolved spectral information and demonstrate the selective excitation of the edge modes. These results pave the way for future study of optical control and many-body physics in polaritonic systems.

Zusammenfassung

Polaritonen sind Quasiteilchen, die aus einer Superposition von Photonen und Exzitonen bestehen und in Halbleiterebenen innerhalb eines optischen Hohlraums erzeugt werden können. In dieser Masterarbeit wird ein System aus mehreren Halbleiterebenen untersucht, die über eine einzelne photonische Hohlraummode miteinander wechselwirken. Durch eine impulsabhängige komplexe Phase in der Kopplung zwischen den Exzitonen und dem Lichtfeld erhält das System nicht-triviale topologische Eigenschaften. Insbesondere entstehen chirale Randmoden, die durch optisches Pumpen in der Nähe des Probenrandes angeregt werden können. Wir simulieren die Dynamik dieses getriebenen Systems im Rahmen der semiklassischen Näherung mithilfe einer dissipativen Gross-Pitaevskii-Gleichung. Dies erlaubt die Untersuchung des topologisch geschützten chiralen Transports entlang des Randes einer endlichen Probe. Weiterhin betrachten wir die Dynamik der topologischen Polaritonen in einem Gittermodell, mit dessen Hilfe wir zeitabhängige Spektraldichten berechnen und damit die selektive Anregung der Randmoden zeigen können. Diese Ergebnisse legen die Grundlage für die weitere Untersuchung von optischer Kontrolle und Vielteilcheneffekten in Polaritonsystemen.

Contents

List of figures	7
Notation reference	9
1 Introduction	11
2 Physical background	13
2.1 Exciton-polaritons in semiconductor cavities	13
2.2 Topological properties of matter	16
2.2.1 Berry phase, connection, and curvature	16
2.2.2 Quantum Hall effect and Chern number	18
2.2.3 Numerical calculation of Berry curvature and Chern numbers	19
3 Topological polariton model	23
3.1 Free model with one semiconductor layer	23
3.2 Free model with multiple semiconductor layers	28
4 Lattice model and edge states	33
4.1 General lattice model	33
4.2 Tight-binding model on a square lattice	34
4.3 Cylindrical lattice geometry	38
4.4 Time-propagation of the driven lattice model	41
4.4.1 Equations of motion	41
4.4.2 Coherent states and semi-classical approximation	43
5 Numerical simulation and results	45
5.1 Semi-classical dynamics	45
5.1.1 Driven dissipative Gross-Pitaevskii equation	46
5.1.2 Dynamics of the single-layer model	48
5.1.3 Dynamics of the multilayer model	51
5.2 Time-resolved spectroscopy for the lattice model	53

Contents

6	Conclusion and outlook	57
A	Origin of the phase-winding exciton-photon coupling	59
B	Computational notes	61
B.1	Simultaneous diagonalization of Hermitian matrices	61
B.2	Discretizing the Fourier transform	62
	Bibliography	65
	Acknowledgments	73

List of figures

2.1	Semiconductor cavity setup	14
2.2	Illustration of Eq. (2.28) for computing the local Chern field	21
2.3	Example implementation of the method of Fukui et al. for computing the Chern number	22
3.1	Band structure of the single-layer model	24
3.2	Pseudo-spin on the sphere	25
3.3	Pseudo-spin and band gap for the single-layer model	26
3.4	Berry curvature for the single-layer model	26
3.5	Berry curvature for the two-layer model	30
4.1	Band structure of the lattice model	36
4.2	Chern field of the lattice model	37
4.3	Topological phases of the lattice model with respect to $\omega_{X,0}$ and m_X	37
4.4	Lattice model with cylindrical boundary conditions	38
4.5	Band structure of the cylindrical lattice model	40
4.6	Band structure around the topological gap for varying number of y layers.	41
5.1	Exciton potential and driving profile	47
5.2	Chiral propagation of polariton population in the driven single-layer system	49
5.3	Propagation of polariton population for $m = 0$	50
5.4	Propagation of polariton population around an impurity	51
5.5	Fraction of the photon population near the boundary	52
5.6	Comparison of the time evolution of edge and bulk population for $L = 1$ and $L = 2$	53
5.7	Spectral density of the driven system	55
5.8	Spectral density within the topological gap	56

Notation reference

1. The sets of natural, integer, real, and complex numbers are denoted by \mathbb{N} , \mathbb{Z} , \mathbb{R} , and \mathbb{C} , respectively. The positive integers are denoted by \mathbb{N}_+ .
2. The imaginary unit is i . The complex conjugate of $z \in \mathbb{C}$ is denoted by z^* , the real (imaginary) part by $\operatorname{Re} z$ ($\operatorname{Im} z$), the absolute value by $|z|$, and the principal branch of the argument by $\operatorname{Arg} z = \operatorname{Im} \operatorname{Log} z \in [0, 2\pi)$.
3. For integer ranges we will write $[n, m]_{\mathbb{Z}} := \{k \in \mathbb{Z} \mid n \leq k \leq m\} = [n, m] \cap \mathbb{Z}$ where $m, n \in \mathbb{Z}$.
4. Vectors will usually be denoted by bold italic symbols \mathbf{v} . Unit vectors will be marked with a check \check{v} and \check{e}_μ denotes the canonical unit vector in μ direction. The euclidean norm of a vector \mathbf{v} is written as $\|\mathbf{v}\| := \sqrt{\sum_j |v_j|^2}$ or just v .
5. Matrices will usually be denoted by bold symbols \mathbf{A} . The $n \times n$ identity matrix is written as \mathbf{I}_n or \mathbf{I} , if the dimension is clear from context. For matrices \mathbf{A}, \mathbf{B} we denote
 - a) the transpose by \mathbf{A}^\top ;
 - b) the conjugate transpose by \mathbf{A}^\dagger ;
 - c) the direct sum by

$$\mathbf{A} \oplus \mathbf{B} = \begin{pmatrix} \mathbf{A} & \mathbf{0} \\ \mathbf{0} & \mathbf{B} \end{pmatrix};$$

- d) unitary equivalence (i.e., the existence of a unitary matrix \mathbf{U} such that $\mathbf{A} = \mathbf{U}^\dagger \mathbf{B} \mathbf{U}$) by $\mathbf{A} \sim \mathbf{B}$.
6. The Pauli matrices are

$$\boldsymbol{\sigma}^x := \begin{pmatrix} 0 & 1 \\ 1 & 0 \end{pmatrix}, \quad \boldsymbol{\sigma}^y := \begin{pmatrix} 0 & -i \\ i & 0 \end{pmatrix}, \quad \boldsymbol{\sigma}^z := \begin{pmatrix} 1 & 0 \\ 0 & -1 \end{pmatrix}.$$

We will also use the formal vector of Pauli matrices $\vec{\boldsymbol{\sigma}} := (\boldsymbol{\sigma}^x, \boldsymbol{\sigma}^y, \boldsymbol{\sigma}^z)^\top$.

List of figures

7. The set of complex Hermitian $n \times n$ matrices is written as

$$\mathcal{H}_n := \{\mathbf{A} \mid \mathbf{A}^\dagger = \mathbf{A}\} \subseteq \mathbb{C}^{n \times n}.$$

8. Quantum mechanical operators will usually be marked with a hat \hat{a} .

9. We will use units with $\hbar = 1$ throughout this thesis.

1 Introduction

Strongly-coupled light-matter systems are of central importance in the realm of condensed matter physics. Light fields can be tuned experimentally to high degrees of precision and over a wide range of frequencies and amplitudes, which makes them a versatile tool in the study of chemical and solid state systems. Results obtained from spectroscopy have informed many of the theoretical developments in understanding the structure of matter [1]. It is also possible to alter the properties of solids by optical means, allowing the study of a diverse range of equilibrium and non-equilibrium phenomena. This includes light-induced superconductivity [2] and topological phases [3, 4].

In semiconductor cavities [5], strong coupling of the photon cavity modes to elementary electronic excitations, called *excitons*, gives rise to light-matter quasiparticles known as *exciton-polaritons* [6, 7]. They possess strongly non-linear properties derived from the constituent excitons while the coupling to the light field allows for experimental control and probing. Among the effects observed in such systems are Bose-Einstein condensation and superfluidity [8, 9, 10], vortex formation [11], four-wave mixing [12], and bright and dark solitons [13, 14], in part mirroring similar experimental developments in the field of ultra-cold quantum gases [15]. Polaritonic devices have possible technological applications, such as the realization of all-optical logical elements [16] and routers [17], which could be useful as building blocks for quantum computing and simulation [18].

Another subject which has received considerable interest in recent times are topological properties of solids [19, 20, 21]. In particular, several works are aiming at the realization of topological insulators in photonic systems. For instance, Haldane and Raghu [22, 23] have proposed a scheme to create a topological bandstructure in an otherwise trivial system via optical driving, leading to so-called Floquet topological insulators.

In 2015, various publications [24, 25, 26] have suggested a setup in which the coupling between exciton and photon modes, both topologically trivial by themselves, gives rise to non-trivial topology featuring chiral edge states. A stable scheme for topologically protected chiral transport of polariton population would provide another useful piece for the toolbox of polaritonic devices. In a similar vein, Peano et al. [27] have studied topologically protected chiral transport in a kagomé lattice of optomechanical arrays.

1 Introduction

In a recent publication, Klemmt et al. [28] have presented an experimental realization of chiral polariton transport based on the theoretical proposals of Refs. [25, 26], demonstrating the feasibility of creating and controlling topological polaritons in real-world systems.

The goal of this thesis is to study the properties of the chiral edge states in the model of Karzig et al. [24] and how they can be selectively excited via optical driving. We will discuss the microscopic structure of the topological polariton model and show results of numerical simulations of chiral transport in a driven bulk system.

The rest of this thesis is structured as follows: In Chapter 2, we will briefly review some fundamental concepts regarding semiconductor cavities and topological properties of matter. In Chapter 3, we will introduce the polariton model at the heart of this thesis and discuss its topological properties as well as an extension to multiple semi-conductor layers. In Chapter 4, we will introduce a tight-binding lattice version of the topological polariton model, allowing us to study band structure and edge states. Further, we will introduce a driven time-dependent version of the lattice model and discuss its time evolution in the semi-classical picture. In Chapter 5, we will present a selection of results of a numerical simulation of the continuous bulk system using the driven dissipative Gross-Pitaevskii and discuss the optical excitation of chiral edge modes. We will also show time-resolved spectroscopy results for the driven lattice model. Finally, we will conclude in Chapter 6.

2 Physical background

This chapter will introduce and give references for several physical concepts that will be used throughout the rest of this thesis.

2.1 Exciton-polaritons in semiconductor cavities

In an optical cavity, photons are trapped between reflecting surfaces. For the physical setup that motivates the models studied in this thesis, the cavity consists of two parallel planar reflectors normal to the z or cavity axis. The reflectors are separated by a distance L_z which is usually of the order of micrometers or nanometers, in which case the cavity is referred to as microcavity or nanocavity. Typically, the reflectors are assumed to be either perfect metallic mirrors (the so-called Fabry-Pérot cavity) [5] or *distributed Bragg reflectors (DBRs)* [9]. A DBR consist of several layers of semiconducting materials with alternating index of refraction. This structure causes destructive interference between transmitted waves, almost completely eliminating the transmission of light over a range of wavelengths called the stop band. The cavity modes are populated with photons by optical pumping. The lifetime of the cavity photons is finite and typically of the order of several to hundreds of picoseconds [10]. A typical setup is shown in Fig. 2.1.

The reflectors impose boundary conditions on the electromagnetic field in the cavity. For the Fabry-Pérot cavity they have the form

$$\check{\mathbf{e}}_n \times \mathbf{E} = 0 \quad \text{and} \quad \check{\mathbf{e}}_n \cdot \mathbf{B} = 0 \quad (2.1)$$

where $\check{\mathbf{e}}_n$ is the unit vector normal to the reflecting plane and \mathbf{E} and \mathbf{B} are the electric and magnetic field, respectively. Making a plane-wave ansatz for the solution of Maxwell's equations inside the cavity, the boundary conditions restrict the z component of the wave vector to

$$q_z = \frac{\pi\nu}{L_z} \quad (2.2)$$

where $\nu \in \mathbb{N}$ and L_z is the distance between the reflectors. The values of the projection of the wave vector to the x - y plane $\mathbf{q}_\perp := (q_x, q_y)^\top$ are unrestricted, as long as an infinite extent of the cavity in x and y direction is assumed. The photon dispersion is given by (recall that $\hbar = 1$)

$$\omega_C(\mathbf{q}) = c\sqrt{q_\perp^2 + q_z^2} \quad (2.3)$$

2 Physical background

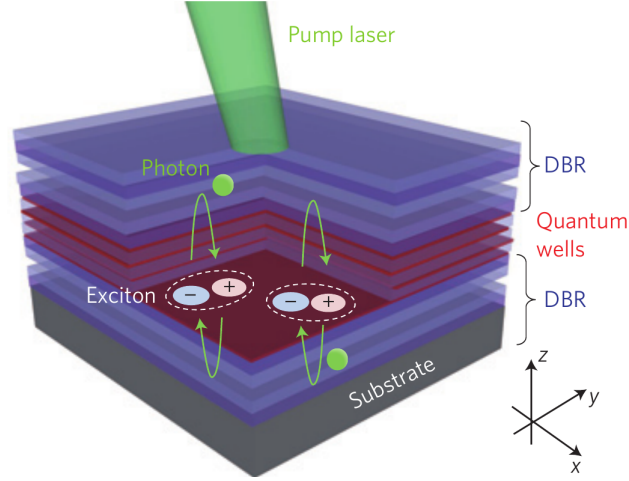


Figure 2.1 | Semiconductor cavity setup as described in the text. Several isolated quantum wells are placed between two distributed Bragg reflectors (DBRs). The cavity photons are populated by optical pumping and couple via dipole interaction to excitons within the planar quantum wells which have the same in-plane momentum q_{\perp} . Image by Byrnes, Kim, and Yamamoto [10].

Reprinted by permission from Springer Nature Customer Service Centre GmbH: Nature Physics, Byrnes, Kim, and Yamamoto, "Exciton-polariton condensates," Copyright 2014.

where c is the speed of light within the medium. For small q_{\perp} (taking q_z to be constant), we can expand

$$\omega_C(q_{\perp}) \approx \omega_{C,0} + \frac{q_{\perp}^2}{2m_C}. \quad (2.4)$$

This shows that the photons obtain a finite effective mass m_C within the x - y plane which is proportional to the quantized out-of-plane momentum q_z . Explicitly,

$$\omega_{C,0} = cq_z \quad \text{and} \quad m_C = \frac{q_z}{c}. \quad (2.5)$$

This photon mass is typically several orders of magnitude smaller than the exciton mass [7, 9].

In order to build a *semiconductor cavity* [9], several layers of a semiconducting material are placed between the reflectors. These layers are separated by a material with a larger band gap, so that the layers are effectively isolated from each other. The confinement potential has the form of a quantum well (QW) in z direction.

We will now introduce the concept of *excitons*, following the review by Deng, Haug, and Yamamoto [9] and the textbook by Combescot and Shiau [29]. An elementary excitation from the ground state of a solid is given by exciting a single electron from the valence into the conduction band. This process leaves a hole in the valence band. The energy associated with the creation of such a pair is very small in a metal. To produce this excitation in a semiconductor, larger energies of the order of several electron volt are required [29]. Electron and hole have opposite charge

and therefore attract each other through the Coulomb force. This can lead to the formation of a bound pair which can be treated as a quasi-particle called a *Wannier exciton*. In a simplified picture, this is analogous to the hydrogen atom, where an electron and a proton are bound together by the Coulomb interaction [5]. “The binding energy of a semiconductor exciton is of the order of 10 meV to 100 meV and its Bohr radius is about 10 Å to 100 Å, extending over tens of atomic sites in the crystal” [9].

Let $\hat{v}_{\mathbf{q}}^\dagger$ and $\hat{c}_{\mathbf{q}}^\dagger$ be valence-band hole and conduction electron creation operators of crystal momentum \mathbf{q} , respectively. Then, the exciton creation operator of center-of-mass momentum \mathbf{Q} is given by [9]

$$\hat{a}_{\mathbf{Q},\nu}^\dagger = \sum_{\mathbf{q},\mathbf{q}'} \delta_{\mathbf{Q},\mathbf{q}+\mathbf{q}'} \phi_\nu \left(\frac{m_h \mathbf{q} - m_e \mathbf{q}'}{m_h + m_e} \right) \hat{c}_{\mathbf{q}}^\dagger \hat{v}_{\mathbf{q}'}^\dagger. \quad (2.6)$$

Here, $\phi_n(\mathbf{q})$ is the Fourier transform of the hydrogen-like wavefunction of relative motion of the bound electron-hole pair with quantum number ν . The constants m_e and m_h are the electron and hole masses, respectively. Assuming $m_e = m_h$ and introducing the relative coordinate $\mathbf{q}_- := \frac{1}{2}(\mathbf{q} - \mathbf{q}')$, this can be brought into the form

$$\hat{a}_{\mathbf{Q},\nu}^\dagger = \sum_{\mathbf{q}_-} \phi_\nu(\mathbf{q}_-) \hat{c}_{\mathbf{q}_- + \mathbf{Q}/2}^\dagger \hat{v}_{\mathbf{q}_- - \mathbf{Q}/2}^\dagger. \quad (2.7)$$

Excitons are *composite bosons*, i.e., quasiparticles consisting of two fermions that approximately obey the bosonic canonical commutation relations. Explicitly, exciton operators satisfy [29]

$$[\hat{a}_{\mathbf{Q},\nu}, \hat{a}_{\mathbf{Q}',\nu'}] = 0, \quad (2.8)$$

$$[\hat{a}_{\mathbf{Q},\nu}, \hat{a}_{\mathbf{Q}',\nu'}^\dagger] = \delta_{\mathbf{Q}\mathbf{Q}'} \delta_{\nu\nu'} - \hat{D}_{\mathbf{Q},\nu;\mathbf{Q}',\nu'}, \quad (2.9)$$

The *deviation operators* $\hat{D}_{\mathbf{Q},\nu;\mathbf{Q}',\nu'}$ correspond to the exchange of fermions between two composite bosons. They are commonly neglected with the argument that their contributions are small unless the average inter-particle spacing approaches the order of the exciton Bohr radius which corresponds to high exciton densities [9]. However, Combescot and Shiau [29] point out that they can still play an important role in the many-body physics of Wannier excitons outside this limit. We will treat excitons as bosonic particles for the remainder of this thesis. The extent of the semiconductor QWs in the cavity direction is assumed to be of the order of the exciton Bohr radius. This confines their motion to a plane and allows us to treat the system as two-dimensional in the models we will discuss here.

Excitons have a non-zero dipole moment which couples them to the electric field of the cavity light modes. Neglecting resonance-broadening mechanisms due to impurities and exciton-phonon interaction, an exciton state with momentum \mathbf{q} is coupled only to cavity photons with the same in-plane momentum [5]. Within the rotating-wave approximation the exciton-photon interaction

2 Physical background

is bilinear [18]. Thus, it can be written in the form

$$\hat{H}_{XC} = \sum_{\mathbf{q}} g(\mathbf{q}) \hat{a}_{X,\mathbf{q}}^\dagger \hat{a}_{C,\mathbf{q}} + \text{H.c.} \quad (2.10)$$

where now \hat{a}_X^\dagger (\hat{a}_C^\dagger) denotes an exciton (photon) creation operator. The prefactor is usually assumed to be a real constant $g(\mathbf{q}) = g_0$ given by the exciton-photon dipole interaction strength [9]. The non-trivial topological properties of the model studied in this thesis arise from adding a momentum-dependent complex phase to $g(\mathbf{q})$, which we will discuss in more detail in Sect. 3.1 and Appendix A.

2.2 Topological properties of matter

In general terms, topological properties of physical systems are those properties that are invariant under a suitable class of continuous transformations. They play a role in many different kinds of physical systems. In solid state physics, the band structure of periodic Hamiltonians can be classified in terms of topological quantum numbers [21, 30, 31]. In quantum gases, gauge fields akin to electromagnetism can be created for neutral particles using Berry phase effects [32], giving rise to the study of artificial gauge fields [33, 34, 35, 36]. Further, topological properties are important in the theory of magnetic skyrmions [37]. A more mathematical treatment of the concepts discussed here in the framework of differential geometry is given by Nakahara [38].

2.2.1 Berry phase, connection, and curvature

Consider a general finite-dimensional Hamiltonian $\mathbf{H}(\mathbf{q}) \in \mathcal{H}_N$ which depends continuously on a parameter $\mathbf{q} \in \mathcal{Q}$ from some M -dimensional manifold \mathcal{Q} . In the context of spatially periodic systems in condensed matter physics, \mathbf{q} is usually the lattice momentum [31]. However, the same treatment is possible for Hamiltonians depending on position [33] or other continuous variables. Due to Hermiticity, this matrix has a full set of real eigenvalues $(\epsilon_j(\mathbf{q}))_{j=1}^N$ with orthonormal eigenvectors $(\mathbf{w}_j(\mathbf{q}))_{j=1}^N$. We will assume both ϵ_j and \mathbf{w}_j to be continuously differentiable functions of \mathbf{q} in the remainder. Also, we assume the absence of band crossings and degeneracies in the spectrum of $\mathbf{H}(\mathbf{q})$ for now, i.e., $\epsilon_j(\mathbf{q}) \neq \epsilon_{j'}(\mathbf{q})$ for all $j \neq j'$. However, the more general case will also be discussed below.

The orthonormality condition requires by definition $\langle \mathbf{w}_i(\mathbf{q}) | \mathbf{w}_j(\mathbf{q}) \rangle = \delta_{ij}$ and thus the normalization $\mathbf{w}_j(\mathbf{q}) = 1$. This still only determines the eigenvectors up to a complex phase, i.e., if $\mathbf{H}(\mathbf{q})\mathbf{w}_j(\mathbf{q}) = \epsilon_j(\mathbf{q})\mathbf{w}_j(\mathbf{q})$, then this also holds for $\mathcal{T}_\chi \mathbf{w}_j(\mathbf{q}) := e^{i\chi(\mathbf{q})}\mathbf{w}_j(\mathbf{q})$ where $\chi(\mathbf{q}) \in \mathbb{R}$. In other words, the eigenvectors possess a separate U(1) gauge freedom at each \mathbf{q} .

The *Berry connection* $\mathbf{A}^j(\mathbf{q})$ is a vector of dimension M with components

$$A_\mu^j(\mathbf{q}) := -i\langle \mathbf{w}_j(\mathbf{q}) | \partial_\mu \mathbf{w}_j(\mathbf{q}) \rangle \quad (2.11)$$

for $j \in [1, N]_{\mathbb{Z}}$ and $\mu \in [1, M]_{\mathbb{Z}}$. By a slight abuse of notation, this is usually written as

$$\mathbf{A}^j(\mathbf{q}) = -i\langle \mathbf{w}_j(\mathbf{q}) | \nabla_{\mathbf{q}} \mathbf{w}_j(\mathbf{q}) \rangle. \quad (2.12)$$

It contains information on the U(1) gauge and transforms under a differentiable phase change as

$$\mathcal{T}_\chi \mathbf{A}^j(\mathbf{q}) = \mathbf{A}^j(\mathbf{q}) - i\nabla_{\mathbf{q}} \chi(\mathbf{q}). \quad (2.13)$$

One can then define the *Berry curvature* as

$$F_{\mu\nu}^j(\mathbf{q}) := \partial_\mu A_\nu^j(\mathbf{q}) - \partial_\nu A_\mu^j(\mathbf{q}). \quad (2.14)$$

The Berry curvature is gauge independent. In $M = 3$ dimensions, the Berry curvature tensor has three independent components which can be computed in analogy to the magnetic field via $\nabla_{\mathbf{q}} \times \mathbf{A}^j(\mathbf{q})$. In $M = 2$ dimensions, the Berry curvature has only one independent component which we write as

$$F^j(\mathbf{q}) := F_{12}^j(\mathbf{q}) = \partial_1 A_2^j(\mathbf{q}) - \partial_2 A_1^j(\mathbf{q}). \quad (2.15)$$

So far, we have introduced the Berry connection and curvature as abstract quantities, emerging from the structure of the eigenstates of a parameter-dependent Hamiltonian. However, the effects arising from this structure can have measurable physical consequences. Berry [32] pointed out in a seminal paper published in 1984 how they play a role in the adiabatic time-evolution of quantum states. We will briefly summarize this result in the next paragraph, following Berry's publication.

Consider a closed path parametrized by $\mathbf{p}: [0, 1] \rightarrow \mathcal{Q}$, $\mathbf{p}(0) = \mathbf{p}(1)$. For simplicity, we assume $M = 2$, i.e., a two-dimensional parameter space (which is not part of Berry's original argument). If the time evolution is sufficiently slow, it is governed by the adiabatic theorem [39, 40]. Then, if the system is in an eigenstate $\psi(0) = \mathbf{w}_j(\mathbf{p}(0))$ at $t = 0$, it will remain in an instantaneous eigenstate for all times. The time evolution introduces the dynamical phase factor which is given by

$$\phi(t) = \int_0^t \epsilon_j(\mathbf{p}(s)) ds. \quad (2.16)$$

However, the state also acquires the so-called *geometrical phase* or *Berry phase* given by the line integral

$$\gamma_j[\mathbf{p}] = i \oint_{\mathbf{p}} \mathbf{A}^j(\mathbf{q}) \cdot d\mathbf{q} \quad (2.17)$$

over the Berry connection corresponding to the j th eigenstate as defined above along the path \mathbf{p} . Due to Stoke's theorem, this phase can also be written as the integral

$$\gamma_j[\mathbf{p}] = i \int_{\mathcal{Q}} F^j(\mathbf{q}) d^2\mathbf{q} \quad (2.18)$$

2 Physical background

of the Berry curvature F^j over the area \mathfrak{A} enclosed by \mathfrak{p} . Since F^j is gauge invariant, so is the Berry phase. Further, it only depends on the path, not on the chosen parametrization (as long as the time-evolution satisfies the conditions of the adiabatic theorem). If the phase is also invariant under continuous deformations of the path, it can be called a *topological phase*.

In conjunction with Berry's publication, Simon [41] presented an interpretation of the Berry phase in terms of holonomy, relating the result to the mathematical fields of topology and differential geometry [38].

The gauge invariance of the geometric phase and its physical implications are the central result of Berry's work. In his publication, he explores its influence on the adiabatic transport of a spin- $\frac{1}{2}$ particle around a band degeneracy and further provides an interpretation of the Aharonov-Bohm effect [42] in terms of the geometric phase. The definition of the Berry curvature (2.14) has the same form as the electromagnetic field tensor with vector potential A^j . This analogy plays a central role in the theory of artificial gauge fields [33, 34, 36].

Wilczek and Zee [43] have discussed the generalization of Berry connection and curvature to the case of multiple degenerate bands. In this case, these quantities are defined for a set of potentially degenerate bands which are still required to be energetically separated from the rest of the spectrum.

2.2.2 Quantum Hall effect and Chern number

In solid state physics, topological effects became prominent with the explanation of the Quantum Hall effect (QHE) in terms of a topologically invariant quantity. We will discuss this briefly, following the review of Hasan and Kane [44]. The QHE refers to the quantization of the Hall conductance of a two-dimensional electron gas in a uniform magnetic field. The Hall conductance has the form

$$\sigma_{\text{H}} = \frac{e^2}{h} C, \quad (2.19)$$

where e and h are the electron charge and Planck constant, respectively, and with an integer number $C \in \mathbb{Z}$. This occurs whenever the Fermi energy lies within a band gap. The effect was first observed experimentally by Klitzing, Dorda, and Pepper [45]. Subsequently, Thouless et al. [30] (TKNN) presented an explicit way to compute this integer. Kohmoto [46] connected this result to the geometrical concepts studied by Berry and Simon. Explicitly, the Hall conductance can be written as

$$\sigma_{\text{H}} = \frac{e^2}{h} \sum_{j \in \text{occ}} C_j, \quad (2.20)$$

where $\text{occ} := \{j \mid \epsilon_j < E_F\}$ denotes the set of bands below the Fermi energy E_F . The integer $C_j \in \mathbb{Z}$ is known as the *Chern number* of the j th band and is given explicitly by

$$C_j = \frac{1}{2\pi} \int_{\mathbb{T}^2} F^j(\mathbf{q}) \, d^2\mathbf{q}. \quad (2.21)$$

It is restricted to integer values due to the geometry of the space of eigenstates over the torical Brillouin zone \mathbb{T}^2 [46]. The Chern number is a topological invariant in the sense that it cannot change under continuous deformations of the spectrum, as long as no band degeneracies are introduced. Thus, if two systems with different bulk Chern numbers are brought into contact, a gap closing must exist at the boundary. This gives rise to the existence of metallic edge states, a property which is known as the *bulk-boundary correspondence* [47, 48]. These states are called topologically protected since they cannot be removed without changing the symmetry of the system or closing the bulk gap [21].

A system can possess different types of topological invariants, depending on its dimension and symmetries [49, 50]. It is possible to classify all possible kinds of topological invariants in terms of these properties, providing what has been called by Kitaev [51] a “periodic table of topological superconductors”. The full classification scheme in terms of ten symmetry classes is known as the *tenfold way* [52].

2.2.3 Numerical calculation of Berry curvature and Chern numbers

In numerical calculations, the eigenvectors are only known at a discrete set of points $\{\mathbf{k}_l\}_{l=1}^N$ in reciprocal space. This leaves the question of how to efficiently compute the Chern number from this data. As a first approach, one could replace the derivative in the definition of the Berry connection (2.11) by a finite difference approximation, e.g.,

$$D_\mu f(\mathbf{k}) := \frac{f(\mathbf{k} + \delta\mathbf{k}_\mu) - f(\mathbf{k})}{\|\delta\mathbf{k}_\mu\|}, \quad (2.22)$$

giving the expression

$$\tilde{A}_\mu^j(\mathbf{k}) = -i \langle \mathbf{w}_j(\mathbf{k}) | D_\mu \mathbf{w}_j(\mathbf{k}) \rangle. \quad (2.23)$$

Here, $\delta\mathbf{k}_\mu$ denotes the difference vector pointing to the next discrete \mathbf{k} point in μ direction. This numerical Berry connection then allows the computation of the Berry curvature which can be summed to get an approximation of the Chern number. However, in order for the expression (2.23) to be well defined, a gauge must be chosen so that the eigenvectors $\mathbf{w}_j(\mathbf{k})$ are smoothly differentiable with respect to \mathbf{k} . This is difficult to achieve in practice, as the phase of the eigenvectors is often the result of implementation choices within the numerical diagonalization routine used.

2 Physical background

The solution to this difficulty is to find a representation of the Berry curvature that does not involve derivatives of the eigenvectors with respect to \mathbf{k} . One such form is the Kubo-type formula [31, Eq. 1.13]

$$F_{\mu\nu}^j = -2 \operatorname{Im} \sum_{l \neq j} \frac{v_{lj}^{(\mu)} v_{jl}^{(\nu)}}{(\epsilon_l - \epsilon_j)^2}, \quad (2.24)$$

where $v_{lj}^{(\mu)} := \langle \mathbf{w}_l | \partial_\mu \mathbf{H} | \mathbf{w}_j \rangle$ are the matrix elements of the velocity operator in the eigenbasis of \mathbf{H} and the sum runs over all other bands. In this equation, the derivatives apply to the Hamiltonian instead of the eigenstates, which makes it particularly useful if those are known analytically. It is also possible, however, to apply a finite difference scheme to the Hamiltonian. Equation (2.24) is manifestly gauge invariant, since $|\mathbf{w}_j\rangle$ and its dual $\langle \mathbf{w}_j|$ both occur together in each term.

An alternative method has been described by Fukui, Hatsugai, and Suzuki [53]. It also does not require specific gauge-fixing conditions and works well even for coarse discretizations of the Brillouin zone. In the following, we will first discuss the case of one band and then a generalization to multiple degenerate bands. Both cases make use of the overlap matrix

$$S_{j_1 j_2}^{(\mu)}(\mathbf{k}_l) := \langle \mathbf{w}_{j_1}(\mathbf{k}_l) | \mathbf{w}_{j_2}(\mathbf{k}_l + \delta \mathbf{k}_\mu) \rangle. \quad (2.25)$$

We assume the \mathbf{k} -points to be known on an equally-spaced square grid over the Brillouin zone.

For the case of a single band j , we define the link variable

$$U_\mu^j(\mathbf{k}_l) := \frac{S_{jj}^{(\mu)}(\mathbf{k}_l)}{|S_{jj}^{(\mu)}(\mathbf{k}_l)|}, \quad (2.26)$$

In the following, the band index j will be suppressed for readability. Since $U_\mu(\mathbf{k}_l)$ is a complex number of unit norm, it is completely defined by the phase

$$\phi_\mu(\mathbf{k}_l) := \operatorname{Arg} U_\mu(\mathbf{k}_l). \quad (2.27)$$

Define now the lattice field strength

$$\begin{aligned} \tilde{F}(\mathbf{k}_l) &:= \operatorname{Arg} [U_1(\mathbf{k}_l) U_2(\mathbf{k}_l + \delta \mathbf{k}_1) U_1(\mathbf{k}_l + \delta \mathbf{k}_2)^{-1} U_2(\mathbf{k}_l)^{-1}] \\ &= \phi_1(\mathbf{k}_l) + \phi_2(\mathbf{k}_l + \delta \mathbf{k}_1) - \phi_1(\mathbf{k}_l + \delta \mathbf{k}_2) - \phi_2(\mathbf{k}_l), \end{aligned} \quad (2.28)$$

which is exactly the phase acquired by moving around a single plaquette in clockwise direction starting at \mathbf{k}_l (Fig. 2.2). Now, the Chern number can be computed as the sum of these phases over the whole \mathbf{k} -space lattice,

$$\tilde{C} = \frac{1}{2\pi} \sum_l \tilde{F}(\mathbf{k}_l). \quad (2.29)$$

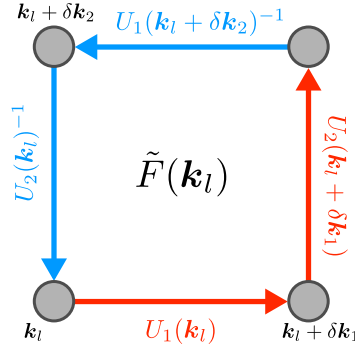


Figure 2.2 | Illustration of Eq. (2.28) for computing the local Chern field $\tilde{F}(\mathbf{k}_l)$, which is obtained by accumulating the phase factors $U_\mu^j(\mathbf{k})$ around a plaquette starting at \mathbf{k}_l as shown.

The definition of the Chern number can be generalized to multiple bands [43, 53], which is described here following Aidelsburger [35]. Consider the family of n distinct band indices $\mathbf{j} \in [1, N]_{\mathbb{Z}}^n$ ($j_r \neq j_s$ for $r \neq s$) and define the overlap matrices $\mathbf{W}_\mu^{\mathbf{j}}(\mathbf{k}_l) \in \mathbb{C}^{n \times n}$ by

$$W_{\mu,rs}^{\mathbf{j}}(\mathbf{k}_l) := S_{j_r j_s}^{(\mu)}(\mathbf{k}_l) = \langle \mathbf{w}_{j_r}(\mathbf{k}_l) | \mathbf{w}_{j_s}(\mathbf{k}_l + \delta \mathbf{k}_\mu) \rangle. \quad (2.30)$$

The multi-band analogon of the link variable (2.26) is then given by

$$U_\mu^{\mathbf{j}}(\mathbf{k}_l) := \frac{\det \mathbf{W}_\mu^{\mathbf{j}}(\mathbf{k}_l)}{|\det \mathbf{W}_\mu^{\mathbf{j}}(\mathbf{k}_l)|}, \quad (2.31)$$

which reduces to Eq. (2.26) for $n = 1$. Now, as in the one-band case of Eqs. (2.28) and (2.29), the multi-band Chern number can be computed as

$$\tilde{C}_j = \frac{1}{2\pi} \sum_l \tilde{F}^j(\mathbf{k}_l) \quad (2.32)$$

using

$$\tilde{F}^j(\mathbf{k}_l) = \text{Arg} \left[U_1^j(\mathbf{k}_l) U_2^j(\mathbf{k}_l + \delta \mathbf{k}_1) U_1^j(\mathbf{k}_l + \delta \mathbf{k}_2)^{-1} U_2^j(\mathbf{k}_l)^{-1} \right]. \quad (2.33)$$

Note that the multi-band Chern number remains well-defined even in the presence of degeneracies of the bands in \mathbf{j} , as long as those bands are still energetically separated from the rest of the spectrum.

Figure 2.3 displays an implementation of this algorithm which was used, alongside the numerical evaluation of Eq. (2.24), for the computation of Chern numbers in the next chapter.

2 Physical background

```

1  # Compute the link variable  $U_\mu^j(k)$ 
2  function link_variable_U(w::Array{Complex128, 4})
3      # The eigenvector  $w_j(k_x[l], k_y[m])$  is  $w[l, m, :, j]$ 
4      nx, ny, _, nbands = size(w)
5
6      # Shift  $w_j(k) \rightarrow w_j(k + \delta k_\mu)$  for  $\mu = x, y$ 
7      w_x = circshift(w, (1, 0, 0, 0))
8      w_y = circshift(w, (0, 1, 0, 0))
9
10     U = Array{Complex128}(nx, ny, 2) # Unnormalized link variable
11
12     for ix in 1:nx, iy in 1:ny
13         # Compute the overlap matrix  $W_\mu^j(k)$ 
14         W = Array{Complex128}(nbands, nbands, 2)
15         for ib1 in 1:nbands, ib2 in 1:nbands
16             W[ib1, ib2, 1] = vecdot(w[ix, iy, :, ib1], w_x[ix, iy, :, ib2])
17             W[ib1, ib2, 2] = vecdot(w[ix, iy, :, ib1], w_y[ix, iy, :, ib2])
18         end
19         # Compute the unnormalized link variable
20         for  $\mu$  in 1:2
21             U[ix, iy,  $\mu$ ] = det(W[:, :,  $\mu$ ])
22         end
23     end
24
25     return U ./ abs.(U) # Return normalized link variable
26 end
27
28 # Compute the Chern field  $F^j(k)$ 
29 function chern_field_F(U::Array{Complex128, 3})
30     U_x = U[:, :, 1]
31     U_y = U[:, :, 2]
32     F = U_x .* circshift(U_y, (1, 0)) ./ circshift(U_x, (0, 1)) ./ U_y
33     return imag.(log.(F))
34 end
35
36 # Compute the Chern number  $\tilde{C}^j = \frac{1}{2\pi} \sum_k F^j(k)$ 
37 chern_number_C(F::Array{Float64, 2}) = round(sum(F) / (2 $\pi$ ))

```

Figure 2.3 | Example implementation of the method of Fukui et al. for computing the Chern number. The code is written in the Julia language [54] (version 0.6.2).

3 Topological polariton model

In this chapter, we introduce the key features of the topological polariton model which we will study in the remainder of this thesis. First, we will discuss the single-layer version and then generalize this model to multiple semiconductor layers.

3.1 Free model with one semiconductor layer

Consider a semiconductor quantum well (QW) embedded within an optical cavity. The extent of the QW in z direction is assumed to be constrained such that the system is effectively two-dimensional. For now, the semiconductor is assumed to be infinite in the remaining two dimensions.

The basic Hamiltonian for this model is given by [24]

$$\hat{H}_0 = \sum_{\mathbf{q}} \left[\omega_X(q) \hat{a}_{X,\mathbf{q}}^\dagger \hat{a}_{X,\mathbf{q}} + \omega_C(q) \hat{a}_{C,\mathbf{q}}^\dagger \hat{a}_{C,\mathbf{q}} + [g(\mathbf{q}) \hat{a}_{X,\mathbf{q}}^\dagger \hat{a}_{C,\mathbf{q}} + \text{H.c.}] \right] \quad (3.1)$$

which can be written in matrix form using the vector of operators $\hat{\mathbf{a}}_{\mathbf{q}} := (\hat{a}_{C,\mathbf{q}}, \hat{a}_{X,\mathbf{q}})^\top$ as

$$\hat{H}_0 = \sum_{\mathbf{q}} \hat{\mathbf{a}}_{\mathbf{q}}^\dagger \mathbf{H}(\mathbf{q}) \hat{\mathbf{a}}_{\mathbf{q}}, \quad \mathbf{H}(\mathbf{q}) = \begin{pmatrix} \omega_C(q) & g(\mathbf{q}) \\ g^*(\mathbf{q}) & \omega_X(q) \end{pmatrix}, \quad (3.2)$$

where $\hat{a}_{X,\mathbf{q}}$ ($\hat{a}_{C,\mathbf{q}}$) is the creation operator of an exciton (photon) with in-plane momentum \mathbf{q} . Both photon and exciton operators satisfy bosonic canonical commutation relations¹. The dispersion relations are given by (Fig. 3.1)

$$\begin{aligned} \omega_X(q) &= \omega_{X,0} + \frac{q^2}{2m_X}, \\ \omega_C(q) &= c\sqrt{q^2 + q_z^2} \end{aligned} \quad (3.3)$$

with $q_z = \frac{\pi\nu}{L_z}$ for $\nu \in \mathbb{N}_+$, cavity length L_z , and exciton mass m_X . The complex exciton-photon interaction is characterized by the function

$$g(\mathbf{q}) = g_0 e^{im\theta(\mathbf{q})}. \quad (3.4)$$

¹Though recall that this is an approximation for excitons.

3 Topological polariton model

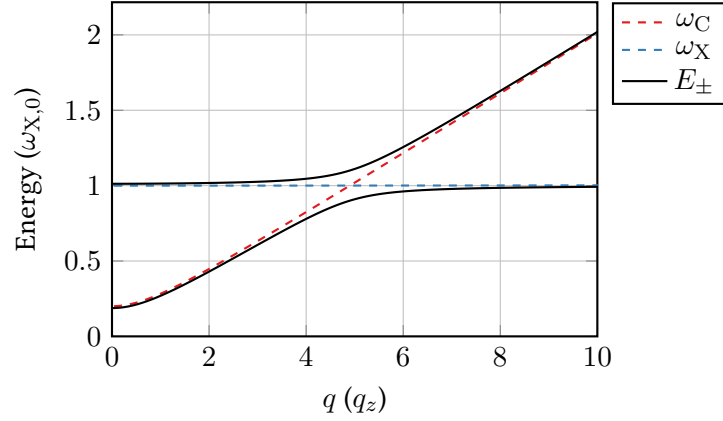


Figure 3.1 | Cavity-photon and exciton dispersions (3.3) (dashed lines), together with the upper and lower polariton bands (solid lines) obtained by diagonalizing $\mathbf{H}(\mathbf{q})$ (3.2). All displayed quantities are radially symmetric with respect to \mathbf{q} .

Here, $\theta(\mathbf{q}) = \text{Arg}(q_x + iq_y)$ is the polar angle of the in-plane vector \mathbf{q} , $m \in \mathbb{Z}$ is the winding number, and g_0 a real constant. The complex phase of the exciton-photon interaction is the main ingredient to achieve non-trivial topology in this model. For $m = 0$ the model reduces to the textbook form of a polaritonic Hamiltonian [7, 9, 29]. Karzig et al. [24] have proposed a way to include this phase in an exciton-photon system, which we briefly review in Appendix A.

The Pauli matrices together with the identity matrix \mathbf{I} form a basis of the 4-dimensional real vector space of 2×2 Hermitian matrices. We can therefore decompose

$$\mathbf{H}(\mathbf{q}) = \begin{pmatrix} \omega_C(q) & g(\mathbf{q}) \\ g^*(\mathbf{q}) & \omega_X(q) \end{pmatrix} = \omega_+(q)\mathbf{I} + \mathbf{d}(\mathbf{q}) \cdot \vec{\sigma}, \quad (3.5)$$

with $\omega_{\pm}(q) := \frac{1}{2}(\omega_C(q) \pm \omega_X(q))$ and the vector of Pauli matrices $\vec{\sigma} := (\sigma^x, \sigma^y, \sigma^z)^\top$. The coefficients of the Pauli matrices are given in polar coordinates $\mathbf{q} = q(\cos(\theta), \sin(\theta))^\top$ by the vector

$$\mathbf{d}(\mathbf{q}) = \begin{pmatrix} g_0 \cos(m\theta) \\ -g_0 \sin(m\theta) \\ \omega_-(q) \end{pmatrix} \in \mathbb{R}^3. \quad (3.6)$$

It has the norm

$$d(q) = \sqrt{g_0^2 + \omega_-^2(q)}. \quad (3.7)$$

Define the normalized vector $\check{\mathbf{d}} := \mathbf{d}/d$, which is referred to as *pseudo-spin* [3]. The behavior of $\check{\mathbf{d}}$ around the origin is shown in Fig. 3.2b. The eigenvectors of \mathbf{H} only depend on \mathbf{d} (since ω_+ just gives a constant energy shift) and are simultaneous eigenvectors of the *helicity operator* $\check{\mathfrak{H}} := \check{\mathbf{d}} \cdot \vec{\sigma}$

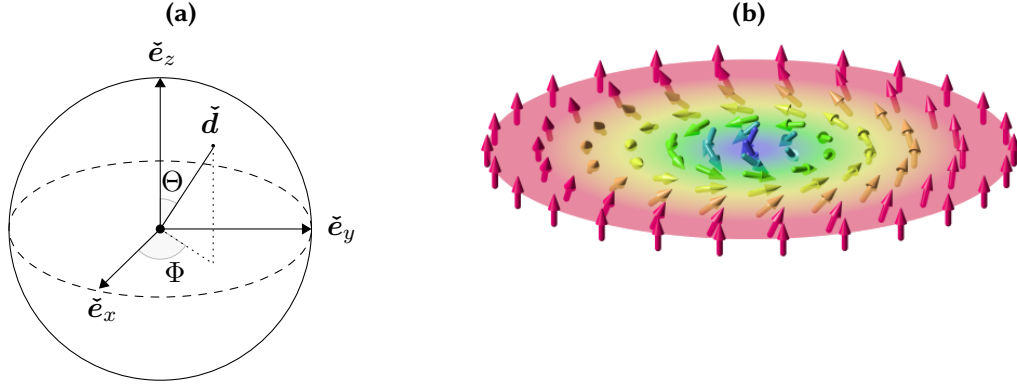


Figure 3.2 | **a** Pseudo-spin vector $\check{\mathbf{d}}$ parametrized in spherical coordinates on the unit sphere (3.10) with zenith (polar) angle Θ and azimuth angle Φ .
b Qualitative behavior of the pseudo-spin vector around the origin in momentum space. Image by Everschor-Sitte and Sitte [56], released under the CC-BY-SA 3.0 license [57].

with eigenvalues ± 1 . Explicitly, the normalized eigenvectors are given by [55]

$$|\pm, \mathbf{q}\rangle = \frac{\mathbf{I} \pm \check{\mathfrak{H}}(\mathbf{q})}{\sqrt{2(1 \pm \check{d}_z(q))}} \begin{pmatrix} 1 \\ 0 \end{pmatrix} = \frac{1}{\sqrt{2}} \begin{pmatrix} \sqrt{1 \pm \check{d}_z(q)} \\ \pm e^{i\theta} \sqrt{1 \mp \check{d}_z(q)} \end{pmatrix}. \quad (3.8)$$

This shows that the pseudo-spin component $\check{d}_z = \omega_-/d$ (Fig. 3.3) determines the excitonic or photonic content of the bands. Specifically, the lower band is purely excitonic (photonic) for $\check{d}_z(q) = +1$ (-1) and vice versa for the upper band. Since we can write $\mathbf{H} = \omega_+ \mathbf{I} + d\check{\mathfrak{H}}$, the eigenvalues of \mathbf{H} are given by $E_{\pm} = \omega_+ \pm d$ (Fig. 3.1).

The pseudo-spin can be used to compute the Chern number via [3]

$$C_{\pm} = \frac{1}{4\pi} \int d^2 \mathbf{q} \check{\mathbf{d}} \cdot (\partial_1 \check{\mathbf{d}} \times \partial_2 \check{\mathbf{d}}). \quad (3.9)$$

In order to evaluate this integral, we parametrize $\check{\mathbf{d}}$ in spherical coordinates (Fig. 3.2a) as

$$\check{\mathbf{d}}(\mathbf{q}) = \begin{pmatrix} \cos \Phi(\theta) \sin \Theta(q) \\ \sin \Phi(\theta) \sin \Theta(q) \\ \cos \Theta(q) \end{pmatrix}, \quad (3.10)$$

with azimuth and zenith angles given by

$$\begin{aligned} \Phi(\theta) &= -m\theta, \\ \cos \Theta(q) &= \check{d}_z(q) = \frac{\omega_-(q)}{d(q)}, \\ \sin \Theta(q) &= \frac{g_0}{d(q)}. \end{aligned} \quad (3.11)$$

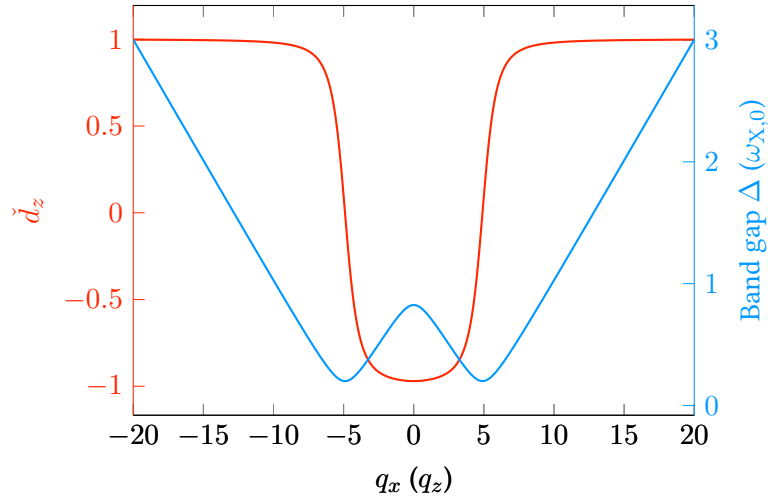


Figure 3.3 | Pseudo-spin component \check{d}_z and band gap $\Delta := 2d$ as functions of momentum along the cut $q_y = 0$. The zero crossings of \check{d}_z occur at the resonance momentum where $\omega_-(q) = 0$. This plot uses the dispersion relations defined in Eq. (3.3) and coupling (3.4) from the text with parameters $c = 1$, $q_z = 0.2$, $m_X = 10^3$, $\omega_{X,0} = 1$, and $g_0 = 0.1$.

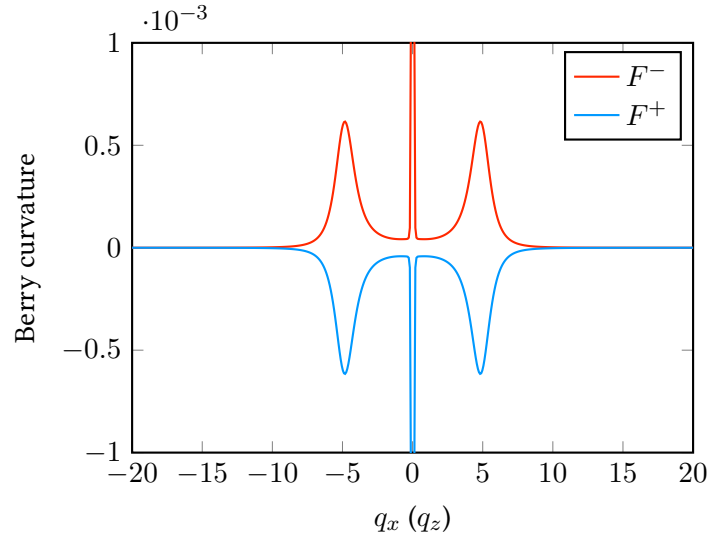


Figure 3.4 | Berry curvature F^\pm as a function of momentum along the cut $q_y = 0$. The only significant contributions come from the singularity at the origin, due to $F^\pm \propto q^{-1}$, and the band inversion at the resonance momentum, due to $F^\pm \propto \partial_q \check{d}_z$ [compare Eq. (3.21)]. The Berry curvature displayed here has been computed by numerically evaluating Eq. (2.24) using a finite-difference approximation for $\partial_\mu \mathbf{H}$. The parameters are the same as in Fig. 3.3.

This gives the Chern number [37]

$$4\pi C_{\pm} = \int_0^{\infty} dq \int_0^{2\pi} d\theta \frac{d\Theta(q)}{dq} \frac{d\Phi(\theta)}{d\theta} \sin \Theta(q) = \pm [\Phi(\theta)]_{\theta=0}^{2\pi} [\check{d}_z(q)]_{q=0}^{\infty}. \quad (3.12)$$

The first factor is $\Phi(2\pi) - \Phi(0) = -2\pi m$. The second factor can be evaluated by rewriting

$$\check{d}_z(q) = \left(1 + \left| \frac{g(q)}{\omega_-(q)} \right|^2 \right)^{-1/2} \text{sign } \omega_-(q). \quad (3.13)$$

For $\lim_{q \rightarrow \infty} \left| \frac{g(q)}{\omega_-(q)} \right| = 0$ this results in $\check{d}_z(\infty) = \lim_{q \rightarrow \infty} \text{sign } \omega_-(q)$. Assuming further that the coupling $g(q)$ vanishes at $q = 0$,² we obtain $\check{d}_z(0) = \text{sign } \omega_-(0)$ and therefore

$$[\check{d}_z(q)]_{q=0}^{\infty} = \text{sign } \omega_-(\infty) - \text{sign } \omega_-(0) \in \{0, \pm 2\}. \quad (3.14)$$

From this equation, we can see that for $C_{\pm} \neq 0$ it is necessary for ω_- to have opposite sign at $q = 0$ and $q \rightarrow \infty$, i.e., for the exciton and photon bands to cross. If this is the case, then the Chern number of the bands is given by the winding number of the coupling,

$$C_{\pm} = \mp m. \quad (3.15)$$

We have thus seen that the coupling (3.4) results in a splitting of the Chern number between upper and lower polariton band, creating a topological system out of two otherwise trivial constituents.

We now present another way of computing the Berry curvature and Chern number directly from the eigenvectors $|\pm, \mathbf{q}\rangle$ of Eq. (3.8). Let $s = \pm 1$ and define $f_s(q) := \sqrt{1 + s\check{d}_z(q)}$. We write the gradient operator in polar coordinates,

$$\nabla_{\mathbf{q}} = \check{e}_q \partial_q + q^{-1} \check{e}_\theta \partial_\theta, \quad (3.16)$$

with the polar basis vectors $\check{e}_q = \cos \theta \check{e}_x + \sin \theta \check{e}_y$ and $\check{e}_\theta = -\sin \theta \check{e}_x + \cos \theta \check{e}_y$ and compute the Berry connection $\mathbf{A}^s = A_q^s \check{e}_q + A_\theta^s \check{e}_\theta$ using

$$A_\theta^s = -i q^{-1} \langle s | \partial_\theta | s \rangle = \frac{-i}{2q} \begin{pmatrix} f_s(q) \\ se^{-im\theta} f_{-s}(q) \end{pmatrix} \cdot \begin{pmatrix} 0 \\ sim e^{im\theta} f_{-s}(q) \end{pmatrix} = \frac{m f_{-s}^2(q)}{2q} \quad (3.17)$$

and

$$A_q^s = -i \langle s | \partial_q | s \rangle = \frac{-i}{2} \begin{pmatrix} f_s(q) \\ se^{-im\theta} f_{-s}(q) \end{pmatrix} \cdot \begin{pmatrix} \partial_q f_s(q) \\ se^{im\theta} \partial_q f_{-s}(q) \end{pmatrix} = 0, \quad (3.18)$$

²This assumption is not true for the model coupling from Eq. (3.4), which is undefined and non-analytic at $q = 0$ due to the complex phase winding. However, Karzig et al. argue that this is an artifact of the simplified model and that for small momenta the system they describe actually has a phase-winding coupling vanishing as q^2 at the origin [24, Appendix A].

3 Topological polariton model

noting that

$$\partial_q f_s = \frac{s}{2f_s} \partial_q \check{d}_z \Rightarrow f_s \partial_q f_s = \frac{s \partial_q \check{d}_z}{2}. \quad (3.19)$$

The Berry connection is thus given by

$$\mathbf{A}^s(\mathbf{q}) = m \frac{f_{-s}^2(q)}{2q} \check{\mathbf{e}}_\theta = m \frac{1 - s \check{d}_z(q)}{2q} \check{\mathbf{e}}_\theta. \quad (3.20)$$

Using $(\nabla_{\mathbf{q}} \times \mathbf{A}^s)_z = q^{-1}[\partial_q(qA_\theta^s) - \partial_\theta A_q^s]$ we obtain the Berry curvature

$$F^s(q) = \frac{-sm \partial_q \check{d}_z(q)}{2q}. \quad (3.21)$$

Integrating the Berry curvature over the whole space yields the Chern number

$$\begin{aligned} C_s &= \frac{1}{2\pi} \int F^s(q) d^2 \mathbf{q} = \frac{1}{2\pi} \int_0^{2\pi} d\theta \int_0^\infty dq q F^s(q) \\ &= \frac{-sm}{2} \int_0^\infty dq \partial_q \check{d}_z(q) = \frac{-sm}{2} [\check{d}_z(q)]_{q=0}^\infty, \end{aligned} \quad (3.22)$$

which is consistent with the result of Eq. (3.12) and thus, together with Eq. (3.14), again implies $C_\pm = \mp m$.

Figure 3.4 shows the Berry curvature computed numerically, which is consistent with the analytic result (3.21). Integrating the numerical curvature F^\pm also yields $C_\pm = \mp m$. Note that the q^{-1} divergence of F^\pm at the origin is due to the singularity of the phase factor $e^{im\theta}$ there. With a coupling of the form $qe^{i\theta} = q_x + iq_y$, which vanishes at the origin and is equivalent to the Dirac monopole, only the peak at the circle of resonance $\{\mathbf{q} \mid \omega_-(q) = 0\}$ remains.

3.2 Free model with multiple semiconductor layers

The model (3.1) can be extended to cover multiple semiconductor layers embedded within the cavity. We assume the separation between the layers is sufficiently large, so that they are not directly coupled, and that all layers couple to the same cavity mode. For the remainder of this thesis, we will denote the cavity mode by C and the exciton layers by X_1, \dots, X_L or, alternatively, use integer indices in $[0, L]_{\mathbb{Z}}$, specifically 0 for C and $0 < l \leq L$ for X_l . If $L = 1$, we will still write X for X_1 .

Let now $\hat{\mathbf{a}}_{\mathbf{q}} := (\hat{a}_{C,\mathbf{q}}, \hat{a}_{X_1,\mathbf{q}}, \dots, \hat{a}_{X_L,\mathbf{q}})^\top$ and define the multi-layer Hamiltonian

$$\hat{H} = \sum_{\mathbf{q}} \hat{\mathbf{a}}_{\mathbf{q}}^\dagger \mathbf{H}(\mathbf{q}) \hat{\mathbf{a}}_{\mathbf{q}}, \quad (3.23)$$

with

$$\mathbf{H}(\mathbf{q}) = \begin{pmatrix} \omega_0(q) & g_1(\mathbf{q}) & \cdots & g_L(\mathbf{q}) \\ g_1^*(\mathbf{q}) & \omega_1(q) & & \\ \vdots & & \ddots & \\ g_L^*(\mathbf{q}) & & & \omega_L(q) \end{pmatrix} = \begin{pmatrix} \omega_0(q) & \mathbf{g}(\mathbf{q}) \\ \mathbf{g}^\dagger(\mathbf{q}) & \boldsymbol{\Omega}_X(q) \end{pmatrix} \in \mathcal{H}_{L+1}. \quad (3.24)$$

The matrix \mathbf{H} is written in the exciton-photon basis $\{|C\rangle, |X_1\rangle, \dots, |X_L\rangle\}$ and is non-zero only on the main diagonal and the first row and column. A matrix of this form is known as an arrowhead matrix [58]. According to Cauchy's interlace theorem [59], the eigenvalues of the principal submatrix $\boldsymbol{\Omega}_X$ interlace the eigenvalues of \mathbf{H} , i.e.,

$$E_{l-1}^\dagger \leq \omega_l^\dagger \leq E_l^\dagger \quad \text{for all } l \in [1, L]_{\mathbb{Z}} \quad (3.25)$$

where $\{\omega_l^\dagger\}_{l=1}^L$ and $\{E_l^\dagger\}_{l=0}^L$ denote the eigenvalues of $\boldsymbol{\Omega}_X$ and \mathbf{H} , respectively, sorted in ascending order. As a consequence, if all exciton layers have the same dispersion $\omega_1 = \dots = \omega_L$, the system exhibits an $(L - 1)$ -fold degenerate band with the exact shape of the exciton dispersion.

To illustrate the structure of the multi-layer Hamiltonian, consider first the case $L = 2$ with equal coupling g and exciton dispersion ω_X , i.e.,

$$\mathbf{H} = \begin{pmatrix} \omega_0 & g & g \\ g^* & \omega_X & 0 \\ g^* & 0 & \omega_X \end{pmatrix}. \quad (3.26)$$

Define the (anti-)symmetric linear combinations of the excitonic basis states

$$|X_\pm\rangle := \frac{1}{\sqrt{2}}(|X_1\rangle \pm |X_2\rangle). \quad (3.27)$$

The antisymmetric state $|X_-\rangle$ is an eigenstate of the Hamiltonian with the eigenvalue ω_X and satisfies $\langle C|\mathbf{H}|X_-\rangle = 0$, i.e., it does not couple to the photon mode and is therefore also called the *dark state*. The symmetric state $|X_+\rangle$ is orthogonal to $|X_-\rangle$ and couples to the photon mode via

$$\langle C|\mathbf{H}|X_+\rangle = \sqrt{2}g. \quad (3.28)$$

In the basis $\mathcal{B} = \{|C\rangle, |X_+\rangle, |X_-\rangle\}$ the Hamiltonian then has the form

$$\mathbf{H}_{\mathcal{B}} = \begin{pmatrix} \omega_0 & \sqrt{2}g & 0 \\ \sqrt{2}g^* & \omega_X & 0 \\ 0 & 0 & \omega_X \end{pmatrix}, \quad (3.29)$$

with a coupling strength enhanced by a factor of $\sqrt{2}$. Since $|X_+\rangle$ is coupled to the photon mode with enhanced strength, it is called the *bright state*. The presence of a bright and a dark state as

3 Topological polariton model

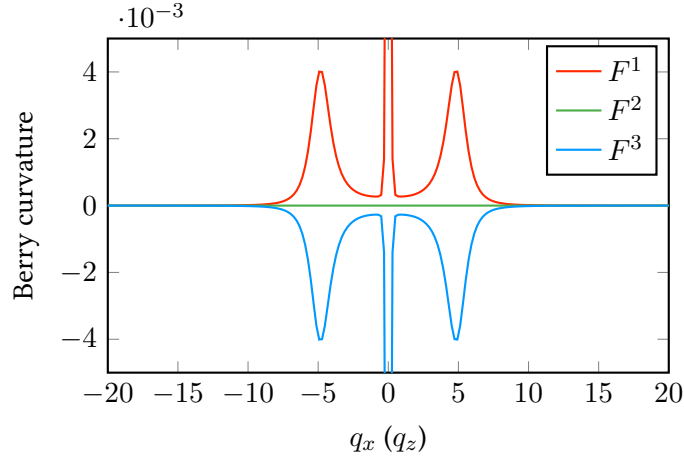


Figure 3.5 | Berry curvature $F^j(q)$ for the two-layer model. F^1 (F^3) corresponds to the lower (upper) polariton band with Chern number $C_{1/3} = \pm 1$ while F^2 corresponds to the band of dark states with $C_2 = 0$. The parameters are the same as for the single-layer case (Figs. 3.3 and 3.4), except for rescaling the coupling strength by a factor of $1/\sqrt{2}$. The Berry curvature displayed here has been computed by numerically evaluating Eq. (2.24) using a finite-difference approximation for $\partial_\mu \mathbf{H}$.

demonstrated in this example is well known in the literature, both in quantum optics [60] and polariton physics [61]. Figure 3.5 shows the Berry curvature of the two-layer system.

We now consider the case of an arbitrary number L of semiconductor layers (but still assuming uniform coupling g and dispersion ω_X). While there is no antisymmetric state for $L > 2$, it is possible to construct the family of states

$$|X_{m/L}\rangle := \frac{1}{\sqrt{L}} \sum_{l=1}^L e^{i2\pi ml/L} |X_l\rangle, \quad m \in [0, L-1]_{\mathbb{Z}}, \quad (3.30)$$

with coefficients given by powers of the L th roots of unity. This construction has been discussed in more detail by Vetter et al. [62] for the study of subradiant states in the Dicke model. Note that $|X_{0/L}\rangle$ is totally symmetric. For $L = 2$ we recover the bright and dark state from above as $|X_{0/2}\rangle = |X_+\rangle$ and $|X_{1/2}\rangle = |X_-\rangle$. Due to the properties of the roots of unity, the states are all orthogonal

$$\langle X_{m/L} | X_{m'/L} \rangle = \delta_{m,m'}. \quad (3.31)$$

The $L - 1$ non-symmetric states are dark,

$$\langle C | \mathbf{H} | X_{m/L} \rangle = 0 \quad m \in [1, L-1]_{\mathbb{Z}}, \quad (3.32)$$

while the symmetric state is bright, with coupling constant

$$\langle C | \mathbf{H} | X_{0/L} \rangle = \sqrt{L}g. \quad (3.33)$$

Thus, the Hamiltonian has two invariant subspaces: the two-dimensional bright subspace

$$\mathcal{H}_{\text{bright}} = \text{span}\{|C\rangle, |X_{0/L}\rangle\} \quad (3.34)$$

and the $(L - 1)$ -dimensional dark subspace

$$\mathcal{H}_{\text{dark}} = \text{span}\{|X_{m/L}\rangle \mid m \in [1, L - 1]_{\mathbb{Z}}\} \quad (3.35)$$

and in the basis $\mathcal{B}' = \{|C\rangle, |X_{0/L}\rangle, \dots, |X_{L-1/L}\rangle\}$ decouples into a direct sum

$$\mathbf{H}_{\mathcal{B}'} = \begin{pmatrix} \omega_0 & \sqrt{L}g \\ \sqrt{L}g^* & \omega_X \end{pmatrix} \oplus \text{diag}(\omega_X, \dots, \omega_X) \quad (3.36)$$

acting on $\mathcal{H}_{\text{bright}} \oplus \mathcal{H}_{\text{dark}}$. In this sense, the bright subspace of the multi-layer system is equivalent to the single-layer model with enhanced coupling $\sqrt{L}g$. In particular, the complex phase of the coupling is still present, so that the bright eigenstates will split into topologically non-trivial polariton bands with Chern numbers determined by the winding number of the coupling. The dark subspace cannot be populated by optical driving and its bands are degenerate, all having the form $\omega_X(\mathbf{q})$, and topologically trivial. For two layers, we have verified this numerically using the same method as for the single-layer case (Fig. 3.5).

It is a natural extension to consider the case of distinct couplings, especially those of the form $g_l = g_0 e^{im_l \theta}$, where the winding number m_l is allowed to differ between the semiconductor layers. However, we have so far not been able to obtain a clear result for this case. The numerical calculation of the Berry curvature and Chern number yield inconsistent results both with the method used for Fig. 3.5 and Fukui's method.

4 Lattice model and edge states

In this chapter we will discuss a tight-binding lattice version of the polariton model (3.1) and show the presence of topological edge states. Furthermore, we will introduce a time-dependent driving to the model and derive the equations of motion that we will use for the numerical simulation in Sect. 5.2.

4.1 General lattice model

Consider first a general lattice model

$$\hat{H} = \sum_{ij} \sum_{rs} t_{rs}(i, j) \hat{a}_{ir}^\dagger \hat{a}_{js} \quad (4.1)$$

where $i, j \in [1, N]_{\mathbb{Z}}$ are lattice site indices and $r, s \in [0, L]_{\mathbb{Z}}$ indices for the local Hilbert space which, in this thesis, consist of a photon mode and L exciton layers. For each pair of sites i, j , we have a coefficient matrix $\mathbf{t}(i, j) = (t_{rs}(i, j)) \in \mathbb{C}^{(L+1) \times (L+1)}$. To make \hat{H} Hermitian, we need $\mathbf{t}^\dagger(i, j) = \mathbf{t}(j, i)$.¹ We assume translation invariance, i.e., $\mathbf{t}(i, j)$ only depends on the distance $\mathbf{r}_{ij} := \mathbf{r}_j - \mathbf{r}_i$ between both lattice sites and thus can be described as a function $\mathbf{t}(\boldsymbol{\delta}_j)$ of all possible lattice translations $\boldsymbol{\delta}_j$. The Hermitian symmetry condition now has the form $\mathbf{t}^\dagger(\boldsymbol{\delta}) = \mathbf{t}(-\boldsymbol{\delta})$. Assuming non-zero $\mathbf{t}(\boldsymbol{\delta})$ only for nearest neighbors (and for $\boldsymbol{\delta} = 0$) is the tight-binding approximation, which yields a sparse matrix structure for the Hamiltonian.

Due to the translation invariance of the system, we can introduce the Fourier transforms of the field operators

$$\hat{b}_{ms} := \frac{1}{\sqrt{N}} \sum_j e^{-i\mathbf{k}_m \cdot \mathbf{r}_j} \hat{a}_{js}. \quad (4.2)$$

and reduce the Hamiltonian (4.1) to

$$\hat{H} = \sum_m \sum_{rs} h_{rs}(\mathbf{k}_m) \hat{b}_{mr}^\dagger \hat{b}_{ms} \quad \text{with} \quad \mathbf{h}(\mathbf{k}_m) = \sum_j \mathbf{t}(\boldsymbol{\delta}_j) e^{i\mathbf{k}_m \cdot \boldsymbol{\delta}_j} \quad (4.3)$$

¹Note that the matrices $\mathbf{t}(i, j)$ themselves do not need to be Hermitian.

4 Lattice model and edge states

where m indexes the reciprocal lattice vectors \mathbf{k}_m within the first Brillouin zone. The momentum-dependent matrix $\mathbf{h}(\mathbf{k}) \in \mathcal{H}_{L+1}$ will be called the *Bloch Hamiltonian* in the following. It is Hermitian, since

$$\mathbf{h}^\dagger(\mathbf{k}) = \sum_j \mathbf{t}^\dagger(\boldsymbol{\delta}_j) e^{-i\mathbf{k}_l \cdot \boldsymbol{\delta}_j} = \sum_j \mathbf{t}(-\boldsymbol{\delta}_j) e^{-i\mathbf{k}_l \cdot \boldsymbol{\delta}_j} = \mathbf{h}(\mathbf{k}). \quad (4.4)$$

The last equality follows by substituting $\boldsymbol{\delta}_j \rightarrow -\boldsymbol{\delta}_j$.

4.2 Tight-binding model on a square lattice

Consider a square lattice with primitive vectors $\{\ell_x, \ell_y\}$. To obtain a tight-binding lattice version of our model (3.1) we assume $L = 1$, i.e., two basis states per lattice site, one photonic and one excitonic. For the hopping matrices, we set

$$\mathbf{t}(0) = \begin{pmatrix} -\mu_C & 0 \\ 0 & -\mu_X \end{pmatrix}, \quad \mathbf{t}(\ell_x) = \begin{pmatrix} t_C & ig_0/2 \\ ig_0/2 & t_X \end{pmatrix}, \quad \mathbf{t}(\ell_y) = \begin{pmatrix} t_C & g_0/2 \\ -g_0/2 & t_X \end{pmatrix}. \quad (4.5)$$

Thus, the model includes local potentials μ_C and μ_X and nearest-neighbor hopping strengths t_C and t_X for the exciton and photon field, respectively. Note that there is no on-site coupling between both fields but only between neighboring sites, with coupling strength proportional to a constant g_0 but with different signs or phases, depending on the direction (x or y) of the corresponding edge. Inserting the hopping matrices (4.5) into Eq. (4.3) gives the Bloch Hamiltonian

$$\mathbf{h}(\mathbf{k}) = \tau_C(\mathbf{k}) \oplus \tau_X(\mathbf{k}) + g_0[\sin(\ell_x k_x) \boldsymbol{\sigma}^x - \sin(\ell_y k_y) \boldsymbol{\sigma}^y] \quad (4.6)$$

with the well-known tight-binding dispersion

$$\tau_l(\mathbf{k}) := 2t_l \sum_{\mu \in \{x,y\}} \cos(\ell_\mu k_\mu) - \mu_l, \quad l \in \{C, X\}. \quad (4.7)$$

The reciprocal lattice vectors for this configuration have the form

$$\mathbf{k}_m = 2\pi \left(\frac{\nu_{m,x}}{N_x \ell_x}, \frac{\nu_{m,y}}{N_y \ell_y} \right) \quad (4.8)$$

where N_μ denotes the number of lattice sites in μ direction and $\nu_{m,\mu} \in [1, N_\mu - 1]_{\mathbb{Z}}$.

The coupling matrix element

$$g(\mathbf{k}) := g_0 [\sin(\ell_x k_x) + i \sin(\ell_y k_y)] \quad (4.9)$$

leads to the same phase winding as displayed by the original coupling term (3.4). Setting

$$t_l := -\frac{1}{2m_l} \quad \text{and} \quad \mu_l := 4t_l - \omega_{l,0}, \quad (4.10)$$

we obtain modified versions of the exciton and photon dispersions (3.3) with the substitution $k_\mu^2 \rightarrow 2 - 2 \cos(\ell_\mu k_\mu)$.

Writing the Bloch Hamiltonian (4.6) in terms of Pauli matrices as in Eq. (3.5) yields

$$\mathbf{h}(\mathbf{k}) = \tau_+(\mathbf{k})\mathbf{I}_L + \mathbf{d}(\mathbf{k}) \cdot \vec{\sigma} \quad (4.11)$$

with $\tau_\pm(\mathbf{k}) = \frac{1}{2}(\tau_C(\mathbf{k}) \pm \tau_X(\mathbf{k}))$ and

$$\mathbf{d}(\mathbf{k}) = \begin{pmatrix} g_0 \sin(\ell_x k_x) \\ -g_0 \sin(\ell_y k_y) \\ \tau_-(\mathbf{k}) \end{pmatrix}. \quad (4.12)$$

This model is, up to prefactors of the terms and the energy shift τ_+ , equivalent to the *Qi-Wu-Zhang (QWZ) model* [63] which is also known as *half Bernevig-Hughes-Zhang (half-BHZ) model* [20], because it has been used by these authors as part of a model to describe the quantum spin-Hall effect in HgTe quantum wells [64]. Weiß [65, Ch. 4] has previously studied nonlinear bosonic transport in the QWZ model.

The bands of the Bloch Hamiltonian (4.11) are given by

$$E_\pm = \tau_+ \pm d = \tau_+ \pm \sqrt{g_0^2[\sin^2(\ell_x k_x) + \sin^2(\ell_y k_y)] + \tau_-^2} \quad (4.13)$$

and are displayed for parameters corresponding to the free model of the previous sections in Fig. 4.1a. The system is gapped unless $d = 0$, which requires $d_x = d_y = 0$ and thus (assuming $g_0 > 0$) restricts the gap closings to the Γ , X, and M points. A gap closing occurs whenever $\tau_-(\mathbf{k}) = 0 \Rightarrow d(\mathbf{k}) = 0$ at one of those points [20]. In any other case, both bands have well-defined Chern numbers which we can compute numerically (compare Fig. 4.2). Just as in the previous sections, we see a Chern number splitting of $C_\pm = \mp 1$ or, if there is no band inversion, $C_\pm = 0$. Figure 4.3 shows the topological phases of the lattice model with respect to the parameters m_X and $\omega_{X,0}$.

Under the assumption $g_0 = t_C - t_X$, our model reduces precisely to the QWZ model and its Chern number only depends on the ratio $u := (\mu_X - \mu_C)/g_0$. Explicitly, it is given by [20]

$$C_\pm = \mp \begin{cases} -1, & u \in [-2, 0], \\ +1, & u \in [0, 2], \\ 0, & |u| > 2. \end{cases} \quad (4.14)$$

For the case of multiple semiconductor layers, we can generalize the hopping matrices to

$$\mathbf{t}(0) = \text{diag}(-\mu_C, -\mu_X, \dots, -\mu_X) \quad (4.15)$$

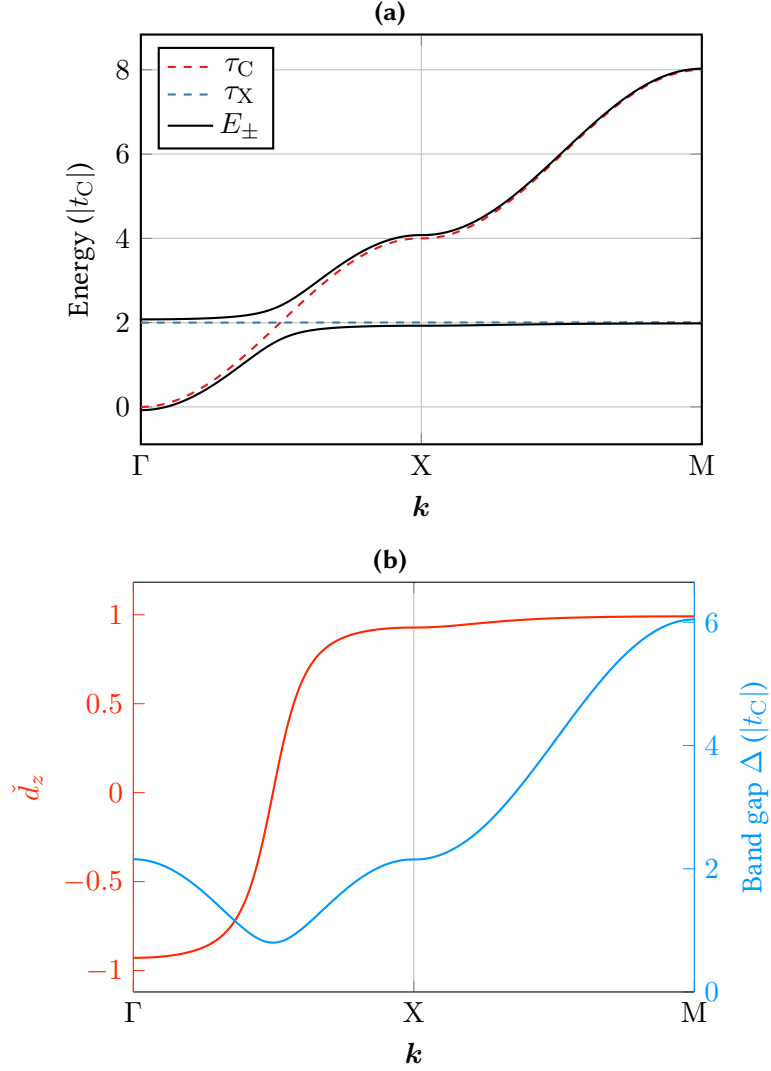


Figure 4.1 | **a** Band structure and **b** exciton-photon component \check{d}_z together with the gap size $\Delta = 2d$ in units of $|t_C|$ for the lattice model. All quantities are plotted along the path through the first Brillouin zone which connects the high-symmetry points $\Gamma = \mathbf{0}$, $X = (\frac{\pi}{\ell_x}, 0)$, and $M = (\frac{\pi}{\ell_x}, \frac{\pi}{\ell_y})$ with straight line segments. The parameters used are $m_X = 10^3 m_C$, $\omega_{X,0} = 2|t_C|$, $\omega_{C,0} = 0$, and $g_0 = 0.4|t_C|$.

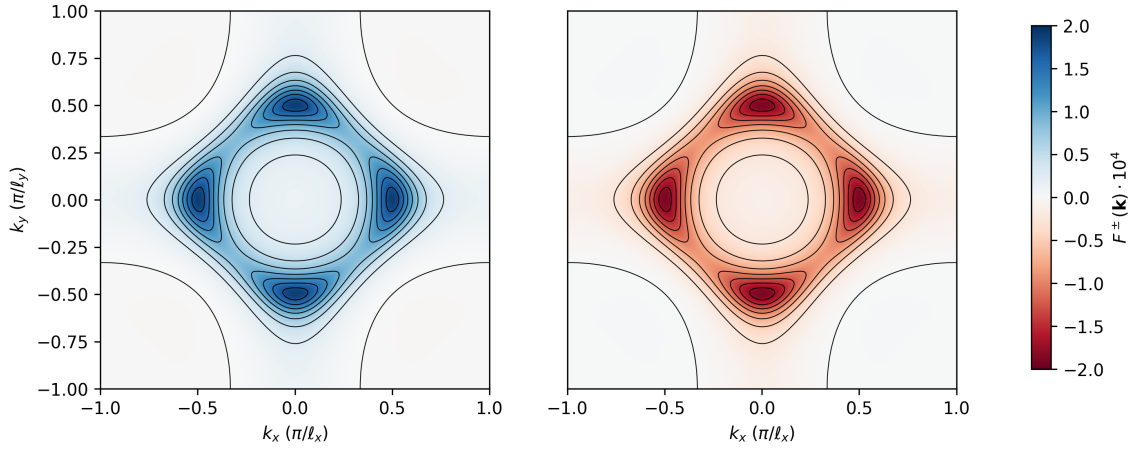


Figure 4.2 | Chern field of the lattice model for the lower (F^-) and upper (F^+) band (left and right panel, respectively), computed using the method of Fukui et al. (Sect. 2.2.3) over the first Brillouin zone discretized on a 512×512 grid. The parameters are the same as in Fig. 4.1. The sum over the Chern fields yields $C_{\pm} = \sum_k F^{\pm}(k) = \mp 1$ for these parameters.

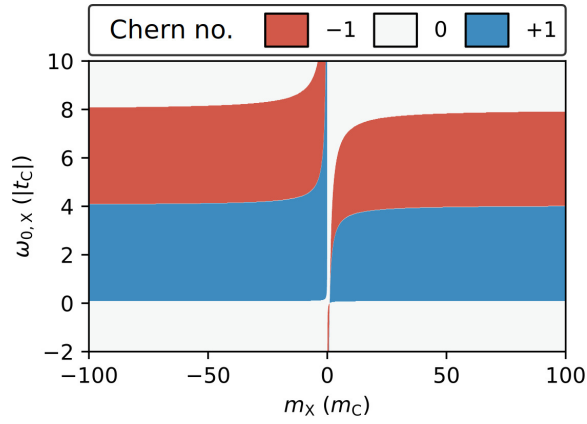


Figure 4.3 | Topological phases of the lattice model with respect to $\omega_{X,0}$ and m_X . The plot shows the Chern number C_- of the lower polariton band, obtained numerically via the method of Fukui et al. For $|m_X| \gg |m_C|$, the exciton dispersion is essentially flat with a constant value of $\omega_{X,0}$, which then determines the Chern number. The critical value of $\omega_{X,0} = 0$ corresponds to a gap closing at the Γ point, where $\tau_C = 0$. The same applies for the critical value $\omega_{X,0} = 4|t_C|$ ($\omega_{X,0} = 8|t_C|$) and the X point (M point).

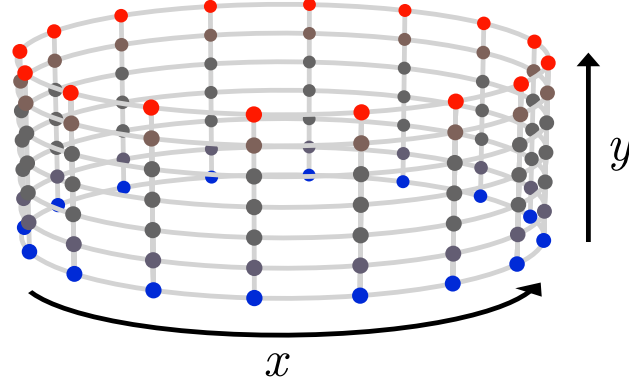


Figure 4.4 | Structure of the lattice model with periodic boundary conditions in x and open boundary conditions in y direction. Since the crystal momentum k_x is still a good quantum number in this setup (i.e., the lattice momentum operator \hat{P}_x still commutes with \hat{H}), we can still classify the spectrum in terms of a band structure with respect to x . Eigenstates can further be classified as bulk or edge states depending on whether there are delocalized over y or exponentially confined to the edges $i_y \in \{1, N_y\}$ (compare Ref. [20, Sect. 6.2]).

$$\mathbf{t}(\ell_x) = \begin{pmatrix} t_C & ig_0/2 & \cdots & ig_0/2 \\ ig_0/2 & t_X & & \\ \vdots & & \ddots & \\ ig_0/2 & & & t_X \end{pmatrix}, \quad \mathbf{t}(\ell_y) = \begin{pmatrix} t_C & g_0/2 & \cdots & g_0/2 \\ -g_0/2 & t_X & & \\ \vdots & & \ddots & \\ -g_0/2 & & & t_X \end{pmatrix}, \quad (4.16)$$

which are arrowhead matrices, just as the multilayer Hamiltonian (3.24) of the free model. Similar to the free model, this results in additional sets of dark bands which exactly follow the uncoupled tight-binding exciton dispersion $\tau_X(\mathbf{k})$ and which are topologically trivial, while a single bright mode still hybridizes with the photonic state to form upper and lower polariton bands with non-zero Chern number.

4.3 Cylindrical lattice geometry

In order to see the presence of edge states, we need to break the lattice translation symmetry and introduce a boundary to the system. Here, we will introduce the boundary in y direction but still use periodic boundary conditions in x direction, which corresponds to a cylindrical topology of the lattice (Fig. 4.4). That way, the lattice momentum k_x remains a viable quantum number, allowing a band structure interpretation of the eigenvalues.

The Hamiltonian can still be written in the form of Eq. (4.1), but with the lattice-site index i only referring to the x direction. Additionally, states are labeled by y -layer indices $i_y \in [1, N_y]_{\mathbb{Z}}$

and local indices $l \in [0, L]_{\mathbb{Z}}$. Introducing the operators

$$\hat{b}_{m,i_y,l} := \frac{1}{\sqrt{N_x}} \sum_{j=1}^{N_x} e^{-ik_m \cdot x_j} \hat{a}_{j,i_y,l}, \quad (4.17)$$

where $k_m := \frac{2\pi m}{N_x \ell_x}$, and assuming again the tight-binding form of Eq. (4.5) yields $\hat{H} = \sum_l \hat{h}(k_l)$ with

$$\hat{h}(k_m) := \sum_{i_y=1}^{N_y} \hat{\mathbf{b}}_{k_m}^\dagger(i_y) \mathbf{h}_{k_m}^{(0)} \hat{\mathbf{b}}_{k_m}(i_y) + \sum_{i_y=1}^{N_y-1} \left[\hat{\mathbf{b}}_{k_m}^\dagger(i_y) \mathbf{t}(\ell_y) \hat{\mathbf{b}}_{k_m}(i_y+1) + \text{H.c.} \right] \quad (4.18)$$

where $\hat{\mathbf{b}}_{k_m}(i_y) := (\hat{b}_{m,i_y,l=0}, \dots, \hat{b}_{m,i_y,l=L})^\top$ and

$$\mathbf{h}_k^{(0)} = \mathbf{t}(0) + \mathbf{t}(\ell_x) e^{ik\ell_x} + \mathbf{t}^\dagger(\ell_x) e^{-ik\ell_x}. \quad (4.19)$$

Unwrapping the indices (i_y, l) in row-major order (i.e., with l being the fastest varying index), we get the explicit block-tridiagonal matrix-form

$$\mathbf{h}(k) = \begin{pmatrix} \mathbf{h}_k^{(0)} & \mathbf{t}(\ell_y) & & 0 \\ \mathbf{t}^\dagger(\ell_y) & \ddots & \ddots & \\ & \ddots & \ddots & \mathbf{t}(\ell_y) \\ 0 & & \mathbf{t}^\dagger(\ell_y) & \mathbf{h}_k^{(0)} \end{pmatrix} \in \mathcal{H}_{(L+1)N_y} \quad (4.20)$$

for the single-particle Hamiltonian. Diagonalizing this matrix numerically, we obtain the band structure shown in Fig. 4.5. This band structure displays $2N_y$ bands. Away from $k_x = 0$, the bands clearly separate into two sets of N_y excitonic and N_y photonic bands, respectively. In the region where the bands cross, there is still a strong excitonic component of the eigenstates around $\omega_{X,0}$, which changes into strongly photonic bands away from this energy. Figures 4.5c and d display the same band structure for a reduced exciton mass, which shows an increase in the size of the topological gap.

Increasing the interaction strength g_0 opens another gap between the two bands crossing the topological gap. This is a finite-size effect caused by the non-zero overlap between the two edge states localized on opposite sides of the system. The overlap results in an avoided crossing in the band structure (see, e.g., Pertsova, Canali, and MacDonald [66] for a similar situation), which vanishes if the number of y layers is increased (Fig. 4.6).

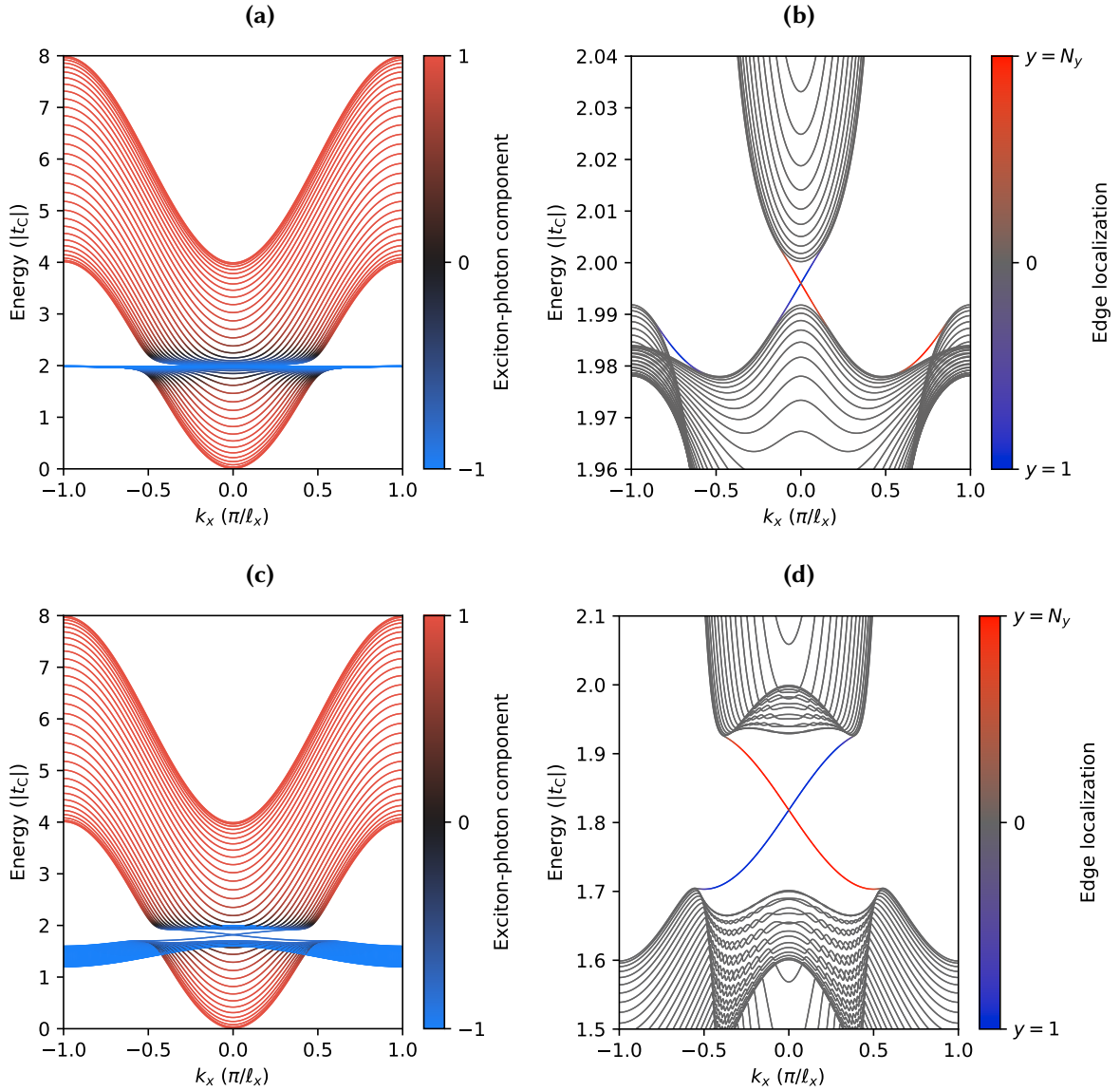


Figure 4.5 | **a** Full band structure of the cylindrical lattice model (4.20) with $N_y = 32$ layers. The bands

are colored according to the photonic or excitonic content of the corresponding eigenstates, from -1 (blue) for purely excitonic to $+1$ (red) for purely photonic bands. The parameters are the same as for Fig. 4.1a, except $m_X = -500m_C$ and $g_0 = 0.2|t_C|$.

b The same band structure as in Panel **a**, zoomed in on the topological gap by rescaling the energy axis. The color indicates the localization of the eigenstates at the edges of the cylinder. States localized close to the $i_y = 1$ ($i_y = N_y$) edge are colored in blue (red). The topological gap around $\omega_{X,0}$ is crossed by two bands of states localized at opposite edges and with opposite slope. Additionally, the band structure features two additional sets of edge states outside the gap around $|k_x| = \frac{3}{4} \frac{\pi}{\ell_x}$.

c–d Same as previous two panels, but with reduced exciton effective mass $m_X = -10m_C$.

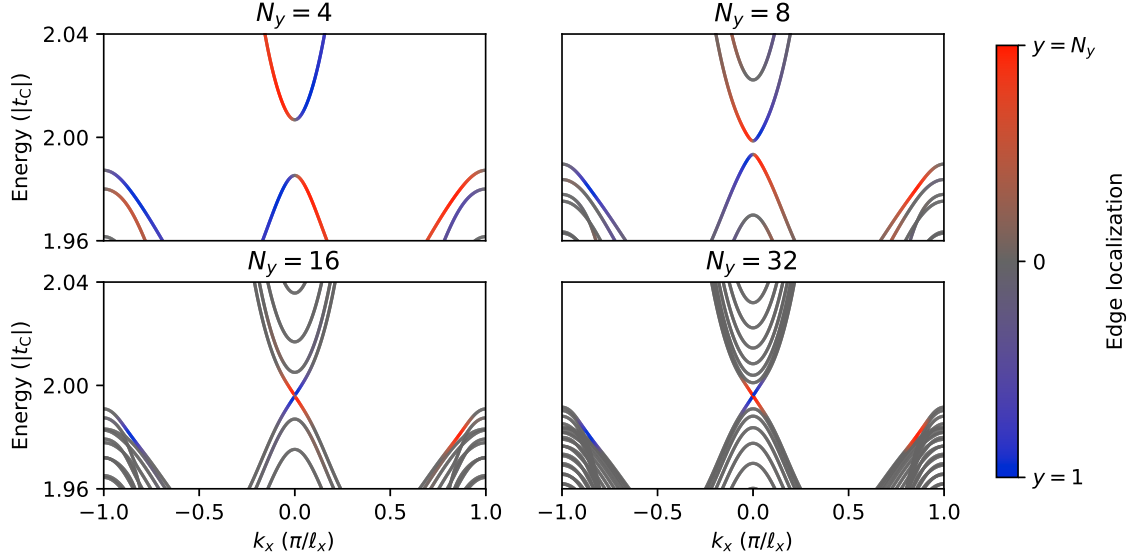


Figure 4.6 | Band structure around the topological gap for varying number of y layers. For small N_y , the avoided crossing between the edge states is clearly visible. This secondary gap vanishes with increasing N_y . The other parameters are the same as for Fig. 4.1a, except for $m_x = -500m_C$.

4.4 Time-propagation of the driven lattice model

In this section, we will introduce a time-dependent driving field of the form $F_i(t)\hat{a}_i^\dagger + \text{H.c.}$ to the lattice Hamiltonian and derive the equations of motion for the two-time single-particle density matrix (or, equivalently, the two-time lesser Green's function). These results will be used for the numerical simulation of the driven lattice model, which is discussed in Sect. 5.2.

4.4.1 Equations of motion

Consider the finite family of bosonic operators $\{\hat{a}_j, \hat{a}_j^\dagger\}_{j=1}^N$ and a Hamiltonian of the form²

$$\begin{aligned} \hat{H} &= \hat{\mathbf{a}}^\dagger \mathbf{h} \hat{\mathbf{a}} + \hat{\mathbf{a}}^\dagger \mathbf{F}(t) + \mathbf{F}^\dagger(t) \hat{\mathbf{a}} \\ &= \sum_{i,j=1}^N \hat{a}_i^\dagger h_{ij} \hat{a}_j + \sum_{i=1}^N \left[F_i(t) \hat{a}_i^\dagger + F_i^*(t) \hat{a}_i \right] \end{aligned} \quad (4.21)$$

with the vector of bosonic operators $\hat{\mathbf{a}} = (\hat{a}_1, \dots, \hat{a}_N)^\top$, the matrix $\mathbf{h} \in \mathcal{H}_N$, and the time-dependent on-site driving $\mathbf{F}(t) \in \mathbb{C}^N$. This general form encompasses the lattice Hamiltonian (4.1).

²For two column vectors $\mathbf{v}, \mathbf{w} \in \mathbb{C}^N$ the scalar product is given by $\mathbf{v}^\dagger \mathbf{w} = \sum_{j=1}^N v_j^* w_j \in \mathbb{C}$ and the dyadic product by $\mathbf{v} \mathbf{w}^\dagger = (v_i w_j^*)_{i,j=1}^N \in \mathbb{C}^{N \times N}$.

4 Lattice model and edge states

We write the operators in the Heisenberg picture, i.e., $\hat{O}^H(t) := \hat{U}(t_0, t) \hat{O}(t) \hat{U}(t, t_0)$ with time propagator $\hat{U}(t, t_0) = \text{T exp} \left(-i \int_{t_0}^t ds \hat{H}(s) \right)$ and where T exp denotes the time-ordered exponential. The operators then satisfy the Heisenberg equation of motion

$$\text{id}_t \hat{O}^H(t) = [\hat{H}(t), \hat{O}^H(t)]. \quad (4.22)$$

For the field operators, the equations of motion are given explicitly by (dropping the superscript H from now on)

$$\text{id}_t \hat{a}_l(t) = \sum_{j=1}^N h_{lj} \hat{a}_j(t) + F_l(t) \quad \Leftrightarrow \quad \text{id}_t \hat{\mathbf{a}}(t) = \mathbf{h} \hat{\mathbf{a}}(t) + \mathbf{F}(t). \quad (4.23)$$

We now look at the single-particle density operators $\hat{\varrho}_{ij} := \hat{a}_j^\dagger \hat{a}_i$ arranged in a matrix $\hat{\varrho} = (\hat{\varrho}_{ij})$. Note the reversed order of the indices, which leads to more natural equations of motion (the equations for \hat{a}_i^\dagger contains additional matrix transposition) and is consistent with the definition of the lesser Green's function, e.g., by Stefanucci and Leeuwen [67]. First, we will only consider the equal-time operator $\hat{\varrho}_{ij}(t) = \hat{a}_j^\dagger(t) \hat{a}_i(t)$. Using the relations

$$\begin{aligned} \hat{\varrho}_{ij}^\dagger &= \hat{\varrho}_{ji}, \\ \hat{\varrho}_{ij} &= \hat{a}_i \hat{a}_j^\dagger - \delta_{ij}, \\ [\hat{\varrho}_{ij}, \hat{a}_l^\dagger] &= \delta_{il} \hat{a}_j^\dagger, \\ [\hat{\varrho}_{ij}, \hat{a}_l] &= -\delta_{jl} \hat{a}_i, \\ [\hat{\varrho}_{ij}, \hat{\varrho}_{lk}] &= \delta_{ik} \hat{\varrho}_{lj} - \delta_{jl} \hat{\varrho}_{ik}, \end{aligned} \quad (4.24)$$

we obtain the equations of motion

$$\begin{aligned} \text{id}_t \hat{\varrho}_{lm} &= \sum_{j=1}^N [h_{lj} \hat{\varrho}_{jm} - \hat{\varrho}_{lj} h_{jm}] + F_l \hat{a}_m^\dagger - F_m^* \hat{a}_l \\ \Leftrightarrow \quad \text{id}_t \hat{\varrho} &= [\mathbf{h}, \hat{\varrho}] + (\mathbf{F} \hat{\mathbf{a}}^\dagger - \hat{\mathbf{a}} \mathbf{F}^\dagger). \end{aligned} \quad (4.25)$$

Without driving, $\mathbf{F} = 0$, this equation of motion (4.25) implies

$$\text{id}_t \hat{n}_i = \sum_{j=1}^N (h_{ij} \hat{\varrho}_{ji} - \hat{\varrho}_{ij} h_{ji}) \quad (4.26)$$

for the density operator $\hat{n}_i := \hat{\varrho}_{ii}$, which suggests the definition of a lattice current

$$\hat{I}_{ij} := 2i \text{Im}(h_{ij} \hat{\varrho}_{ji}) \quad (4.27)$$

so that the following discrete continuity equation holds:

$$\text{d}_t \hat{n}_i + \sum_{j=1}^N \hat{I}_{ij} = 0. \quad (4.28)$$

4.4.2 Coherent states and semi-classical approximation

The expectation values $\mathbf{a}(t) := \langle \hat{\mathbf{a}}(t) \rangle \in \mathbb{C}^N$ and $\boldsymbol{\rho}(t) := \langle \hat{\boldsymbol{\rho}}(t) \rangle \in \mathbb{C}^{N \times N}$ obey the same equations of motion, with the operators replaced by the respective expectations. Note that $\boldsymbol{\rho}$ is proportional to the equal-time lesser Green's function, $\boldsymbol{\rho}(t) = -i\mathbf{G}^<(t, t)$ [67]. All observables which are at most quadratic in the bosonic operators can be expressed in terms of $\hat{\mathbf{a}}$ and $\hat{\boldsymbol{\rho}}$. Thus, if their expectation values are known for some initial state, the complete time evolution can be computed by solving the ODE system given by Eqs. (4.23) and (4.25) which has dimension of the order of N^2 .

When starting from a coherent initial state the time propagation can be simplified even more: Let $\boldsymbol{\alpha} \in \mathbb{C}^N$ and define the corresponding multi-mode coherent state as [68, 69]

$$|\boldsymbol{\alpha}\rangle := \prod_{j=1}^N \hat{D}_j(\alpha_j)|0\rangle \quad (4.29)$$

where $|0\rangle$ is the Fock vacuum and the *displacement operator* $\hat{D}_j(\alpha) := \exp(\alpha\hat{a}_j^\dagger - \alpha^*\hat{a}_j)$ creates a single-mode coherent state. Note that $\hat{D}_j(0) = \text{id}$ and $\langle \boldsymbol{\alpha} | \boldsymbol{\beta} \rangle = \exp(-\|\boldsymbol{\alpha}\|^2/2 + \boldsymbol{\alpha}^\dagger \boldsymbol{\beta} - \|\boldsymbol{\beta}\|^2/2)$ and thus $\langle \boldsymbol{\alpha} | \boldsymbol{\alpha} \rangle = 1$. The coherent states are eigenstates of the bosonic annihilators such that $\hat{a}_j|\boldsymbol{\alpha}\rangle = \alpha_j|\boldsymbol{\alpha}\rangle$. As a consequence, the expectation value of every normal-ordered operator with respect to $|\boldsymbol{\alpha}\rangle$ can be obtained by replacing $\hat{a}_j^{(\dagger)} \rightarrow \alpha_j^{(*)}$.

In a coherent initial state we have $\mathbf{a}(0) = \boldsymbol{\alpha}$ and $\boldsymbol{\rho}(0) = \boldsymbol{\alpha}\boldsymbol{\alpha}^\dagger = (\alpha_i\alpha_j^*)_{i,j=0}^N$. Since the coherent state is fully specified by $\boldsymbol{\alpha}$, the density matrix $\boldsymbol{\rho}$ and thus all observables can be obtained from this vector. Define the *covariance matrix*

$$\boldsymbol{\Gamma} := \boldsymbol{\rho} - \mathbf{a}\mathbf{a}^\dagger \quad \Leftrightarrow \quad \Gamma_{ij} = \langle \hat{a}_j^\dagger \hat{a}_i \rangle - \langle \hat{a}_j^\dagger \rangle \langle \hat{a}_i \rangle, \quad (4.30)$$

which is zero precisely for coherent states. It evolves in time as

$$i\dot{\Gamma}_{lm} = \dot{\rho}_{lm} - a_l \dot{a}_m^* - \dot{a}_l a_m^* = \sum_{j=1}^N [h_{lj}\Gamma_{jm} - \Gamma_{lj}h_{jm}] \quad (4.31)$$

or, in short,

$$i\text{d}_t \boldsymbol{\Gamma} = [\mathbf{h}, \boldsymbol{\Gamma}]. \quad (4.32)$$

The derivative is independent of $\mathbf{F}(t)$ and, since the time-evolution generated by Eq. (4.32) conserves the norm of the covariance matrix, $\boldsymbol{\Gamma}(0) = 0$ implies $\boldsymbol{\Gamma}(t) = 0$ for all times. It follows that if the system is in a coherent state at $t = 0$, it will be in the coherent state given by $\mathbf{a}(t)$ for all times, i.e., the many-body quantum state of the system is fully determined by this field. Assuming $\boldsymbol{\Gamma} = 0$ and propagating only $\mathbf{a}(t)$ leads to an ODE system of size N and is known as the *semi-classical approximation*, which we have found to be exact for the Hamiltonian under consideration here, as long as we start in a coherent state.

This discussion is a special case of the more general theory of Gaussian states [70, 71]. The manifold of Gaussian states is invariant under the time evolution generated by Hamiltonians of up to second degree in the field operators $\{\hat{a}_i, \hat{a}_i^\dagger\}$, such as Eq. (4.21), and for bosons these states are completely defined by \mathbf{a} and $\mathbf{\Gamma}$, in our notation. This, together with Eq. (4.32), implies the exactness of the semi-classical approximation for any coherent initial state. For general Gaussian initial states, i.e., $\mathbf{\Gamma}(0) \neq 0$, it is necessary to also propagate $\mathbf{\Gamma}$ via its equation of motion (4.32).

The previous results also generalize to the two-times density matrix

$$\hat{\rho}_{ij}(t_1, t_2) = \hat{a}_j^\dagger(t_2) \hat{a}_i(t_1). \quad (4.33)$$

More specifically, we find that (compare Stan, Dahlen, and Leeuwen [72] for $\mathbf{F} = 0$)

$$\nabla_{\mathbf{t}} \hat{\rho}(\mathbf{t}) = \begin{pmatrix} \mathbf{h} \hat{\rho}(\mathbf{t}) + \mathbf{F}(t_1) \hat{\mathbf{a}}^\dagger(t_2) \\ -\hat{\rho}(\mathbf{t}) \mathbf{h} - \hat{\mathbf{a}}(t_1) \mathbf{F}^\dagger(t_2) \end{pmatrix} \quad (4.34)$$

where $\mathbf{t} = (t_1, t_2)$ and $\nabla_{\mathbf{t}} = (\partial_{t_1}, \partial_{t_2})^\top$ denotes the gradient with respect to the two time arguments. Further, we have

$$\nabla_{\mathbf{t}} \mathbf{\Gamma}(\mathbf{t}) = \begin{pmatrix} \mathbf{h} \mathbf{\Gamma}(\mathbf{t}) \\ -\mathbf{\Gamma}(\mathbf{t}) \mathbf{h} \end{pmatrix}, \quad (4.35)$$

so that the time evolution preserves the relation

$$\boldsymbol{\rho}(t_1, t_2) = \mathbf{a}(t_1) \mathbf{a}^\dagger(t_2) \quad (4.36)$$

also in the two-time case. This will be relevant for computing spectroscopic data in Sect. 5.2, which requires the lesser Green's function $\mathbf{G}^<(t_1, t_2) = \mathbf{i} \boldsymbol{\rho}(t_1, t_2)$. For $t_1 = t_2$, the directional derivatives $(1, 1)^\top \cdot \nabla_{\mathbf{t}} \hat{\rho}(t, t)$ and $(1, 1)^\top \cdot \nabla_{\mathbf{t}} \mathbf{\Gamma}(t, t)$ reproduce the equal-time equations of motion (4.25) and (4.32), respectively.

5 Numerical simulation and results

In this section we will present results from the numerical simulations of the topological polariton models introduced in the previous chapters. We will start with the study of a bulk system including exciton-exciton interaction and dissipation using a Gross-Pitaevskii-type non-linear Schrödinger equation. To complement this picture, we will discuss time-resolved spectroscopy results obtained from a simulation of the driven lattice model using the equations of motion derived in Sect. 4.4.

5.1 Semi-classical dynamics

In bosonic systems, the semi-classical picture corresponds to replacing the creation and annihilation operators by a complex field, i.e.,

$$a_l(\mathbf{r}, t) := \langle \hat{a}_l(\mathbf{r}, t) \rangle, \quad l \in \{C, X_1, \dots, X_L\}. \quad (5.1)$$

Note that we have now written the field in continuous real space, i.e.,

$$\mathcal{F} \hat{a}_l(\mathbf{r}, t) = \hat{a}_{l,q}(t) \quad (5.2)$$

with the Fourier transform operator \mathcal{F} and the bosonic operators $\hat{a}_{l,q}$ defined as in Sect. 3.1. As we have seen in Sect. 4.4.2, this approximation becomes exact for bilinear Hamiltonians and coherent initial states. Even in the presence of non-negligible interactions, however, the semi-classical picture can be used, which is done successfully in the study of the superfluid phases in ultracold quantum gases [15, 73, 74] and polariton systems [7], among others. The inter-particle interaction corresponds to polynomial terms of fourth degree in the field operators in the Hamiltonian. Specifically, the exciton-exciton interaction written in real space can be described by a contact interaction of the form [7]

$$\hat{H}_{\text{int}} = \frac{g_{XX}}{2} \int d^2\mathbf{r} \hat{a}_X^\dagger(\mathbf{r}) \hat{a}_X^\dagger(\mathbf{r}) \hat{a}_X(\mathbf{r}) \hat{a}_X(\mathbf{r}). \quad (5.3)$$

In order to incorporate these interactions in the semi-classical picture, a mean-field approximation is used, which results in an interaction term of the form

$$H_{\text{int}} = \frac{g_{XX}}{2} \int d^2\mathbf{r} |a_X(\mathbf{r})|^4, \quad (5.4)$$

which contributes to the equation of motion of the field $a_X(\mathbf{r})$ as

$$\mathrm{id}_t a_X(\mathbf{r})\Big|_{\mathrm{int}} = \frac{\delta H_{\mathrm{int}}}{\delta a_X^*(\mathbf{r})} = g_{\mathrm{XX}} |a_X(\mathbf{r})|^2 a_X(\mathbf{r}). \quad (5.5)$$

This term can be interpreted as coming from a density-dependent effective potential $V_{\mathrm{int}}(|a_X(\mathbf{r})|^2)$ and including it in the Schrödinger equation yields what is known as the Gross-Pitaevskii equation (GPE) [74]. The equation of motion further incorporates dissipation via

$$\mathrm{id}_t a_l(\mathbf{r})\Big|_{\mathrm{diss}} = -i\gamma_l a_l(\mathbf{r}). \quad (5.6)$$

The driving discussed in Sect. 4.4 gives rise to a term of the form

$$\mathrm{id}_t a_l(\mathbf{r})\Big|_{\mathrm{driv}} = F_l(\mathbf{r}, t). \quad (5.7)$$

5.1.1 Driven dissipative Gross-Pitaevskii equation

The full equation of motion we simulate has the form of a driven dissipative Gross-Pitaevskii equation (DDGPE)

$$\mathrm{id}_t \mathbf{a}(\mathbf{r}, t) = [\mathcal{F}^{-1} \mathbf{H}(\mathbf{q}) \mathcal{F} + \mathbf{V}(\mathbf{r}) - i\mathbf{\Gamma}] \mathbf{a}(\mathbf{r}, t) + \mathbf{W}(\mathbf{a}(\mathbf{r}, t)) + \mathbf{F}(\mathbf{r}, t) \quad (5.8)$$

with the vector-valued field¹ $\mathbf{a}(\mathbf{r}, t) = (a_0(\mathbf{r}, t), a_1(\mathbf{r}, t), \dots, a_L(\mathbf{r}, t))^\top$. This equation (for $L = 1$) has been used by, e.g., Ballarini et al. [16] and Karzig et al. [24] for the study of polariton dynamics. The matrix $\mathbf{H}(\mathbf{q})$ is the free non-interacting single-particle Hamiltonian (3.24) described in Sect. 3.2, which contains the momentum-dependent dispersion and the phase-winding exciton-photon coupling. In order to apply $\mathbf{H}(\mathbf{q})$ in momentum space, the forward and backward Fourier transforms are computed numerically as written in the equation using the fast Fourier transform implemented in FFTW3 [75] (Sect. B.2). The matrix $\mathbf{V}(\mathbf{r}) := \mathrm{diag}(V_0(\mathbf{r}), \dots, V_L(\mathbf{r}))$ contains the local single-particle potential in each layer. In the following, we will only consider exciton potentials, for which we will use a hexagonal lattice of the form

$$V^X(\mathbf{r}) := -v_X \left(\cos(\kappa_1 x) + \cos(\kappa_1 x/2 + \sqrt{3}\kappa_2 y/2) + \cos(-\kappa_1 x/2 + \sqrt{3}\kappa_2 y/2) \right) \quad (5.9)$$

with reciprocal vector $\boldsymbol{\kappa} \in \mathbb{R}^2$ and potential strength v_X , which is the same as used by Karzig et al. [24]. In order to constrain the fields to the rectangular simulation region $\mathcal{S} = [0, L_x] \times [0, L_y]$, we introduce artificial boundary potential V^{wall} for both exciton and photon fields. The boundary potential takes a constant value significantly larger than the characteristic energies of the system near the boundary of \mathcal{S} . The total potential is thus given by $V_0 = V^{\mathrm{wall}}$ and $V_l = V^X + V^{\mathrm{wall}}$ for $l > 0$ (Fig. 5.1a). The dissipation is controlled by the matrix $\mathbf{\Gamma} := \mathrm{diag}(\gamma_0, \dots, \gamma_L)$ with constants

¹Recall that we use indices $0 \equiv C$ and $l \equiv X_l$ for $0 < l \leq L$, interchangeably.

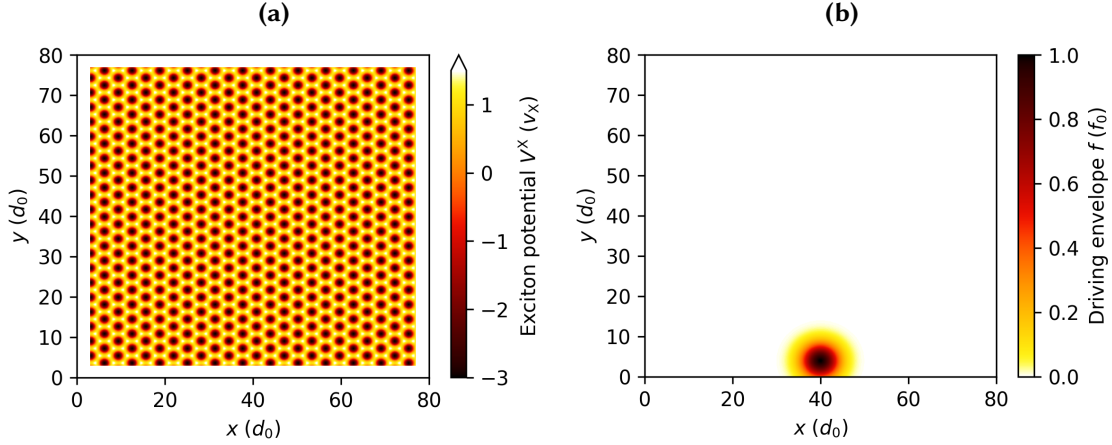


Figure 5.1 | **a** Hexagonal exciton potential (5.9) in units of the potential strength v_X and with $\kappa = (2, 2)d_0^{-1}$ where d_0 is the spatial unit and with potential wall V^{wall} around the simulation region.

b Gaussian driving profile $f(\mathbf{r})$ in units of f_0 for $\sigma_d = 3d_0$. The driving is focused on the point $\mathbf{r}_d = (40, 4)d_0$ close to the boundary of the sample.

$\gamma_l \in \mathbb{R}$. The equation further contains the Gross-Pitaevskii interaction term

$$\mathbf{W}(\mathbf{a}) := g_{XX} (0, |a_1|^2 a_1, \dots, |a_L|^2 a_L)^\top. \quad (5.10)$$

The first component W_0 is zero, since there are no photon-photon interactions. The driving only affects the photon field ($F_l = 0$ for $l > 0$), via

$$F_0(\mathbf{r}, t) := f(\mathbf{r}) \exp(-i\omega_d t) \quad (5.11)$$

with the spatial driving profile $f(\mathbf{r})$, for which we use the Gaussian shape (Fig. 5.1b)

$$f(\mathbf{r}) = f_0 \exp\left(-\frac{\|\mathbf{r} - \mathbf{r}_d\|^2}{2\sigma_d^2}\right). \quad (5.12)$$

The DDGPE as stated here is an ordinary differential equation since the Fourier transform turns the spatial derivatives into algebraic operations. It thus can be solved via standard numerical techniques, such as the Runge-Kutta class of methods. For the simulations described here, we have used the *Runge-Kutta Dormand-Prince (Dopri5)* scheme [76]. Specifically, we have used the implementation of *boost::odeint* [77] for the DDGPE and a custom implementation based on Press [78, 17.2] for the lattice model. Dopri5 is a fifth-order method with an embedded fourth-order scheme which is used to provide an estimate of the (absolute or relative) local truncation error. The step size is adjusted during the time evolution in order to keep this error below a predefined bound. This approach is known as *adaptive step size*.

Our code for solving Eq. 5.8 is written as a C++ library which contains the core functionality and a Python wrapper script which is responsible for setup and post-processing. The output of our simulation is the time-dependent field $\mathbf{a}(\mathbf{r}, t)$ at a fixed set of time steps together with information about the simulation parameters. This data is stored in the NetCDF 4 format [79]. For post-processing we use *xarray* [80] and *dask* [81] for conveniently dealing with multi-dimensional data arrays and *matplotlib* [82] for plotting. Scans over ranges of parameters and several post-processing tasks were run in parallel with the help of *GNU parallel* [83].

5.1.2 Dynamics of the single-layer model

First, we will analyze the behavior of the system for a single semiconductor layer, $L = 1$, as discussed in Sect. 3.1. We can reproduce the results presented by Karzig et al. [24, Fig. 7]: Driving the system with a Gaussian pump pulse centered at the edge of the sample shows the presence of edge states with a chirality determined by the winding number m of the coupling $g_l(\mathbf{q}) = g_0 \exp(i\theta(\mathbf{q}))$, as expected due to the non-zero Chern number (Fig. 5.2). The chirality of the system is determined by the winding number m . Setting $m = -1$ inverts the direction of propagation compared to $m = 1$.

Figure 5.3 shows the behavior of the fields in the topologically trivial case $m = 0$. No chiral edge transport occurs in this case. Instead, both exciton and photon populations spread out symmetrically around the focus of the driving. This is caused primarily by the nonlinear interaction term incorporated in the GPE, because this term acts as an effective potential proportional to $|a_l|^2$ and therefore energetically punishes high densities.

The chiral propagation is resistant to disturbance by obstacles (e.g., impurities in the material), which can be seen in Fig. 5.4.

In order to determine the influence of the driving parameters on the population of the edge mode, we will use the fraction of population located close to the edge. First, we partition the simulation region into bulk and edge regions (Fig. 5.5a) and compute the total population within the edge region as

$$N_l^{(\text{edge})}(t) := \int_{\text{edge}} d^2\mathbf{r} |a_l(\mathbf{r}, t)|^2, \quad l \in \{C, X_1, \dots, X_L\}. \quad (5.13)$$

Let N_l denote the total population. We normalize bulk and edge population to the total population, $\bar{N}_l^{(\text{edge})} := N_l^{(\text{edge})}/N_l$. Comparing bulk and edge population then shows whether the driving is resonant with the edge mode, leading to a larger value of $\bar{N}_l^{(\text{edge})}$. Figure 5.5b shows these quantities for varying driving frequency ω_d and two different values of the interaction strength g_{XX} . We see that the driving is only resonant with the edge mode over a small frequency range, which is consistent with the small size of the topological gap observed for the lattice model in Sect. 4.3.

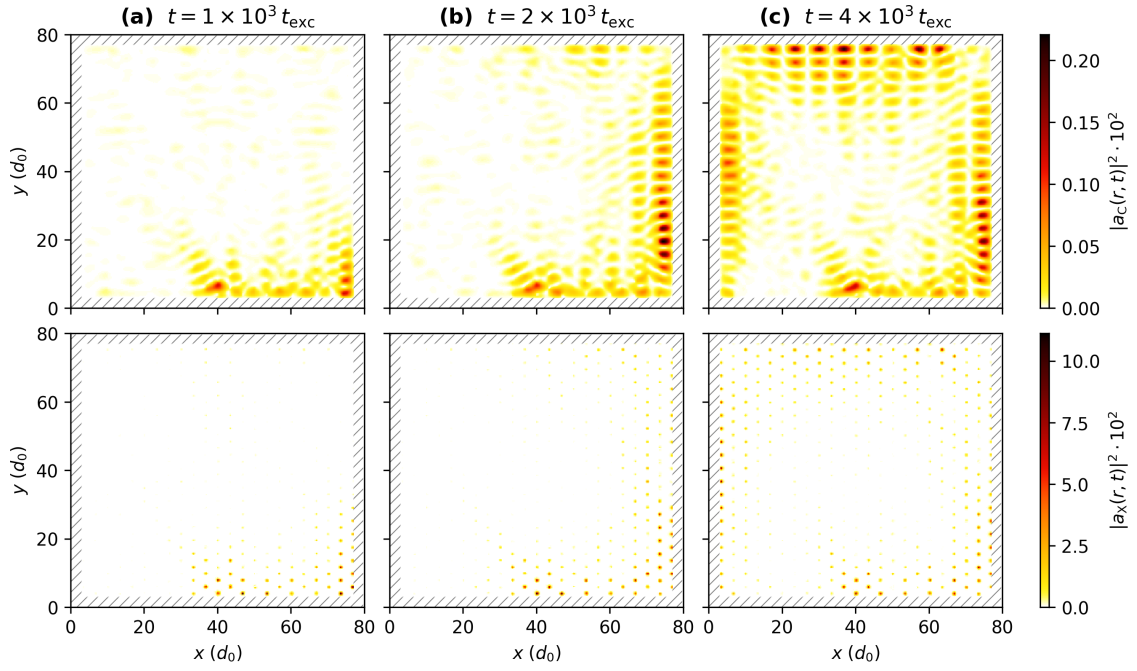


Figure 5.2 | **a–c** Chiral propagation of population in the driven single-layer system for different simulation times. For each time, measured from the start of the driving at $t = 0$, the upper (lower) panel shows the corresponding photon (exciton) population $|a_{C/X}|^2$. The driving is focused on the point $\mathbf{r}_d = (40, 4)d_0$ with a Gaussian profile (5.12), driving frequency $\omega_d = 0.856\omega_{X,0}$, and amplitude $f_0 = 10^{-2}\omega_{X,0}$. Position is given in the computational unit d_0 , which is related to the lattice constant of V^X by $a = 3.86d_0$. The parameters of the potential are $v_X = 0.05\omega_{X,0}$ and $\kappa = (1.88, 1.88)d_0$. The winding number of the exciton-photon coupling is $m = 1$. Time is measured in units of $t_{\text{exc}} := \omega_{X,0}^{-1}$. The hatched region is the support of the boundary potential V^{wall} .

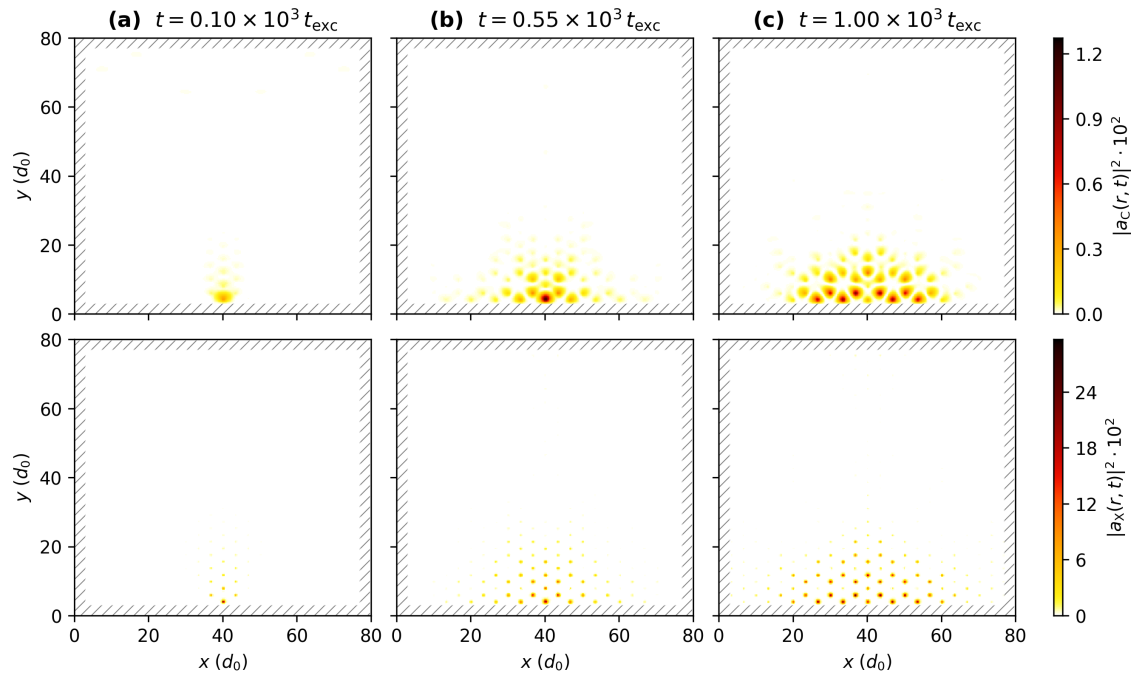


Figure 5.3 | **a–c** Propagation of polariton population for the topologically trivial case $m = 0$. Otherwise, the parameters are the same as for Fig. 5.2. The polariton population spreads symmetrically around the driving focus r_d , driven primarily by the exciton-exciton interaction which imposes an energy cost on high local densities.

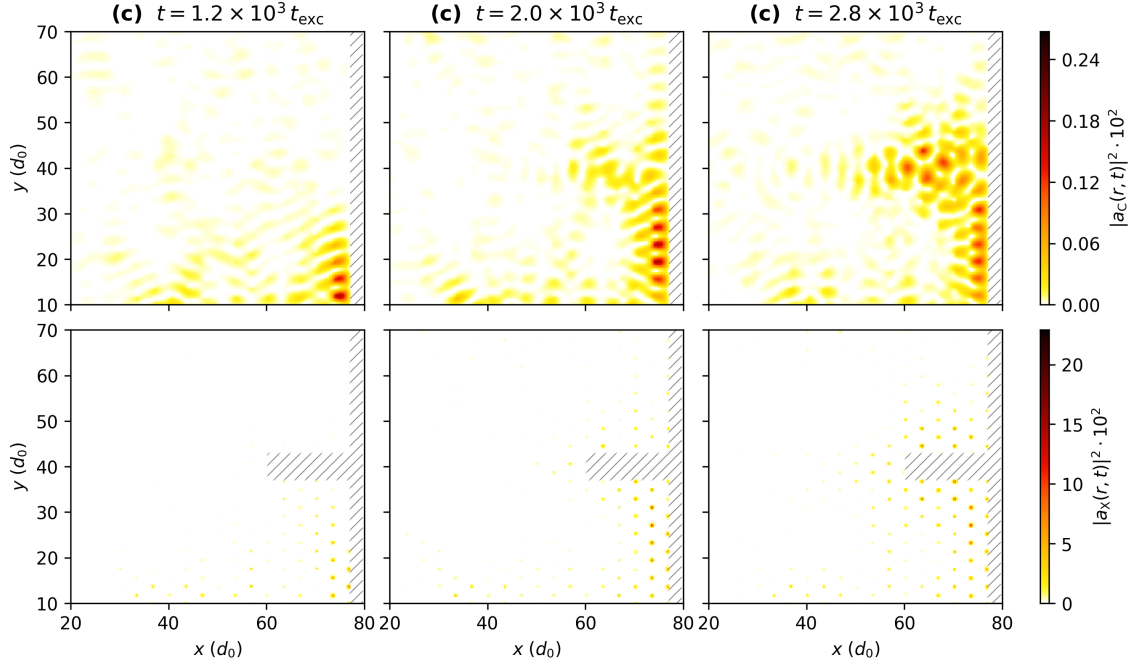


Figure 5.4 | a–c Propagation of the polariton wavefunction around an impurity which is modeled by partially extending the exciton potential wall (hatched region) into the bulk. The parameters are otherwise the same as for Fig. 5.2.

These results illustrate the sensitivity of the system to the choice of driving parameters, which we have also observed to a lesser extent with regard to the driving amplitude and exciton-photon coupling strength. This has made it difficult for us to go beyond the continuous pumping scheme described here and to explore possible technical applications of the chiral transport in the spirit of polaritonic devices.

5.1.3 Dynamics of the multilayer model

In Sect. 3.2 we have discussed how multiple exciton layers, uncoupled among each other, give rise to a subspace of dark states and a single bright state that couples to the photon mode with enhanced strength. This is corroborated by numerical results for the non-interacting case.

We define the population at the edge as in Eq. 5.13 above and the bulk population as the difference $N_l^{(\text{bulk})} := N_l - N_l^{(\text{edge})}$. Further, we define the bright (dark) excitonic field $a_{\pm} := \frac{1}{\sqrt{2}}(a_{X1} \pm a_{X1})$ with the corresponding population $N_{\pm}^{(\text{bulk})}$ and $N_{\pm}^{(\text{edge})}$. In the two-layer case, we choose a rescaled exciton-photon coupling according to Eq. 3.33, i.e., $g'_0 := \frac{1}{\sqrt{2}}g_0$ in order to obtain the same effective bright-state coupling strength as for the single layer.

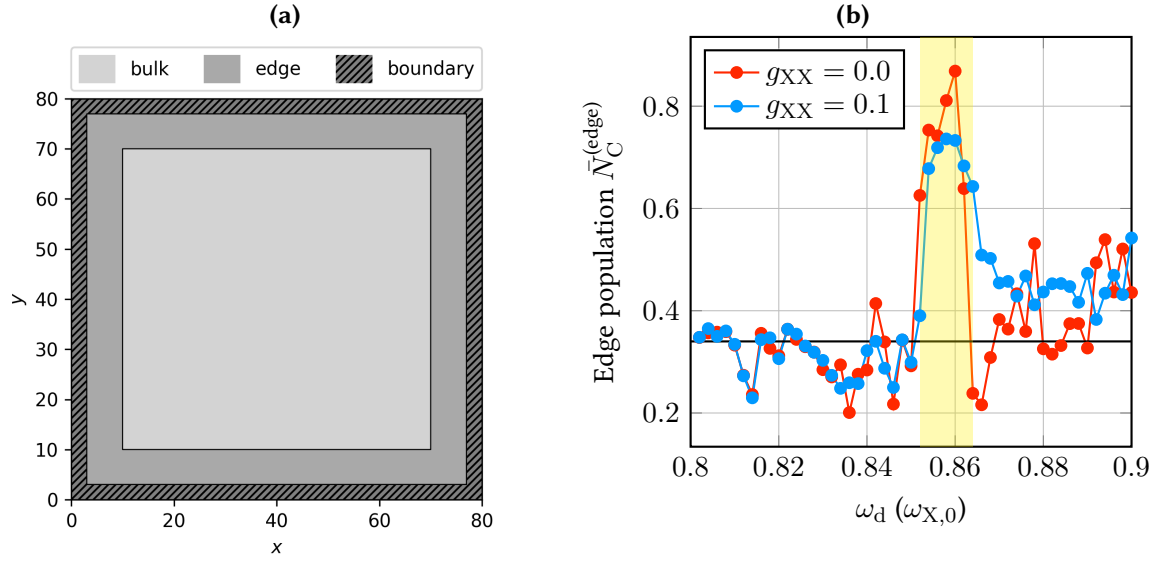


Figure 5.5 | **a** Partition of the simulation region into bulk and edge regions, surrounded by the boundary potential V^{wall} .

b Fraction of the photon population near the boundary $\bar{N}_C^{(\text{edge})}$ after continuously driving the system for a simulation time of $t_{\text{end}} = 4 \times 10^3 t_{\text{exc}}$. In the frequency interval $\omega_d / \omega_{X,0} \in [0.852, 0.864]$ (highlighted region) we see a resonance with a significant fraction of the population located near the boundary of the system. This corresponds to the chiral propagation shown in Fig. 5.2. The horizontal line marks the ratio of the edge region to the total area of inside the boundary, which is approximately 0.34.

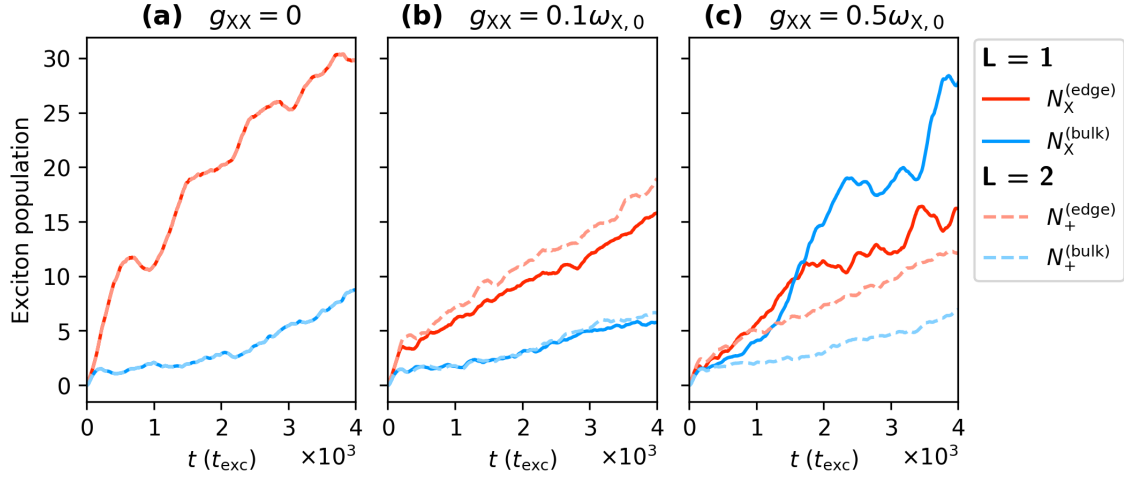


Figure 5.6 | a–c Comparison of the time evolution of edge (red) and bulk (blue) population for $L = 1$ (solid lines) and $L = 2$ (dashed lines) at different exciton-exciton interaction strengths g_{XX} . For the two-layer system, a coupling strength of $g'_0 := \frac{1}{\sqrt{2}}g_0$ is used in order to obtain an effective coupling equivalent to the single layer. The population of the bright state $a_+ := \frac{1}{\sqrt{2}}(a_{X1} + a_{X1})$ is denoted by N_+ . Except for g_0 and g_{XX} , the simulation parameters are the same as in Fig. 5.2.

Figure 5.6 shows the time evolution of bulk and edge population for $L = 1$ and $L = 2$ under these conditions. In the absence of exciton-exciton interaction, the time evolution of the population in the single exciton layer is indeed identical to the bright-state population in the two-layer system. For non-zero g_{XX} , the populations no longer evolve identically but diverge after some time, which happens earlier at higher interaction strength. In both cases, there is no population transferred to the dark state a_- .

5.2 Time-resolved spectroscopy for the lattice model

In the previous section we have discussed the results of the DDGPE simulation, in particular the sensitivity of the chiral edge excitation to the driving frequency. In order to study the effect of the driving on the excitation of the chiral edge states, we will turn our focus to the tight-binding lattice model introduced in Sect. 4.2 with an additional time-dependent driving $\mathbf{F}(t)$ of the form discussed in Sect. 4.4. Specifically, we simulate the model given by [compare Eqs. (4.1) and (4.21)]

$$\hat{H} = \sum_{i,j=1}^N \sum_{l,l'=0}^L t_W(i,j) \hat{a}_{il}^\dagger \hat{a}_{jl'} + \sum_{i=1}^N \sum_{l=0}^L (F_{il}(t) \hat{a}_{il}^\dagger + \text{H.c.}) \quad (5.14)$$

on a square lattice with N sites and with a local Hilbert space of dimension $L + 1$ at each site, representing the photon and exciton degrees of freedom. For the results discussed here, the driving

5 Numerical simulation and results

is restricted to the photon field $l = 0$ and to a single site i_0 , i.e., $F_{il}(t) = f(t)\delta_{l0}\delta_{ii_0}$ and with $f(t) = f_0 e^{-i\omega_d t}$. The hopping matrices are those of the lattice model given in Sect. 4.2. We impose cylindrical boundary conditions as discussed in Sect. 4.3. We will measure the time in units given by the photon hopping parameter, i.e., in units of $t_{\text{hop}} := |t_C|^{-1}$.

In order to explicitly see how the population of the bands is affected by the driving, we look at the time-resolved spectral density (trSD) defined by

$$\mathbf{I}^{(\text{full})}(\omega) := \text{Im} \int d^2t S_{t_p, \sigma_p}(t_1) S_{t_p, \sigma_p}(t_2) e^{i\omega(t_1 - t_2)} \mathbf{G}^<(t_1, t_2). \quad (5.15)$$

This is the same formula as for the photocurrent in time-resolved pump-probe photoemission spectroscopy measurements which has been derived by Freericks, Krishnamurthy, and Pruschke [84] for fermionic systems. For the bosonic system we simulate here, the trSD is used as a tool to observe the effects of the driving with time and energy resolution. The function $S(t)$ describes the shape of the pump pulse, which we assume to be Gaussian,

$$S_{t_p, \sigma_p}(t) := \frac{1}{\sigma_p \sqrt{2\pi}} \exp\left(-\frac{(t - t_p)^2}{2\sigma_p^2}\right). \quad (5.16)$$

The time resolution is provided by varying the probe time t_p . The duration depends on the width σ_p of the Gaussian and determines the spectral resolution of the trSD. A larger probe duration leads to an increase in spectral resolution.

In order to obtain the input for Eq. (5.18), we perform the following steps. First, starting from an vacuum initial state $\mathbf{a}(0) = 0$, the field expectation values \mathbf{a} are propagated by solving the equations of motion (4.23) with the time-dependent driving given above. In order to provide momentum-resolved information, we Fourier transform \mathbf{a} with respect to the periodic lattice coordinate x , giving the field $b_{m, i_y, l}(t)$ [compare Eq. (4.17)]. From this we obtain the two-time lesser Green's function as [compare Eq. (4.36)]

$$G^<(k_m, t_1, t_2) = i \sum_{i_y=1}^{N_y} \sum_{l=0}^L b_{m, i_y, l}(t_1) b_{m, i_y, l}^*(t_2) \quad (5.17)$$

with $k_m = \frac{2\pi m}{N_x \ell_x}$. In order to reduce the amount of information, we have performed a partial trace over $\mathbf{G}^<$ with regard to the y -layer and exciton-photon degrees of freedom and only included the part diagonal in k_m . This gives us the trSD

$$I(\omega, k_m; t_p) = \text{Im} \int d^2t S_{t_p, \sigma_p}(t_1) S_{t_p, \sigma_p}(t_2) e^{i\omega(t_1 - t_2)} G^<(k_m, t_1, t_2). \quad (5.18)$$

The integrand is only computed in a region where the probe shape has non-negligible weight. For the results included here, we have chosen a cutoff beyond a distance of $3\sigma_p$ from t_p .

The momentum-resolved spectral density (Fig. 5.7) shows that the driving excites states at the energy corresponding to ω_d over the whole range of available momenta k_x . This is, however, only

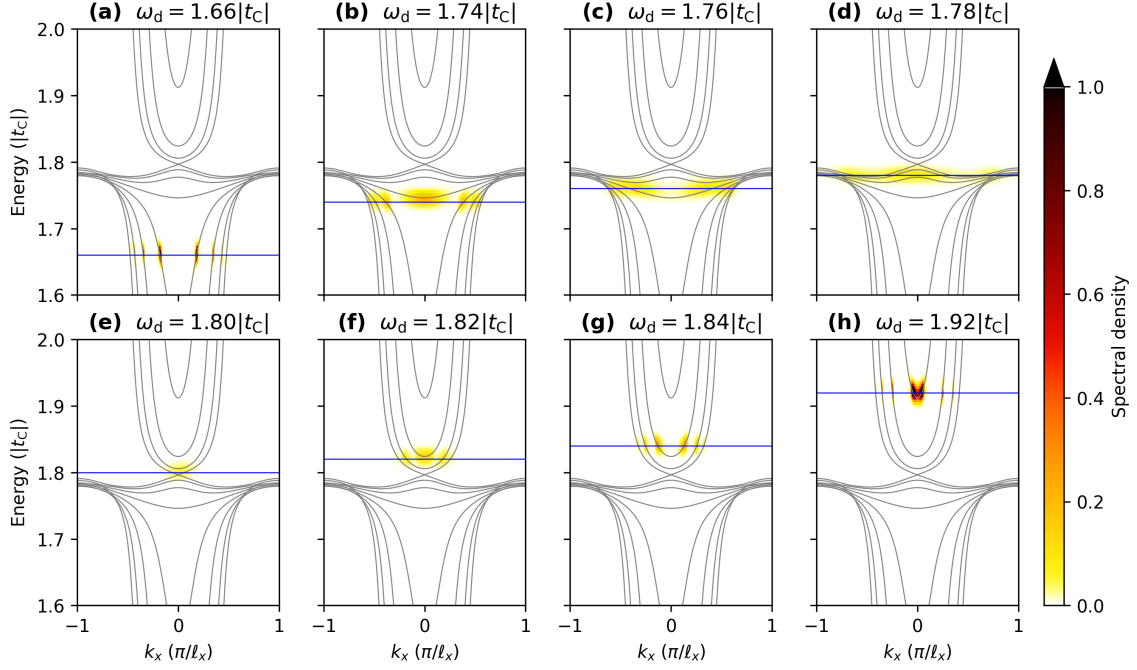


Figure 5.7 | **a–h** Spectral density of the driven system at a fixed probe time $t_p = 350t_{\text{hop}}$ with $\sigma_p = 100t_{\text{hop}}$ for different values of the driving frequency ω_d (blue line) on a $N_x \times N_y = 256 \times 8$ lattice with periodic boundary conditions in y direction. The grey lines show the equilibrium band structure of the model. The other parameters are $m_X = -500m_C$, $\omega_{X,0} = 1.8|t_C|$, $g_0 = 0.2|t_C|$ and the driving amplitude is $f_0 = 0.2|t_C|$.

true for the bulk system. In order to take a closer look at the topological gap, we choose an exciton mass of $m_X = -10m_C$, which significantly increases the size of the gap (compare Fig. 4.5d) and thus reduces the computing time necessary to resolve the bands within the gap. The resulting trSD is shown in Fig. 5.8. Inside the gap, the driving is only resonant with one of the two crossing bands, which fits our observation of unidirectional chiral propagation in the continuous model (Fig. 5.2).

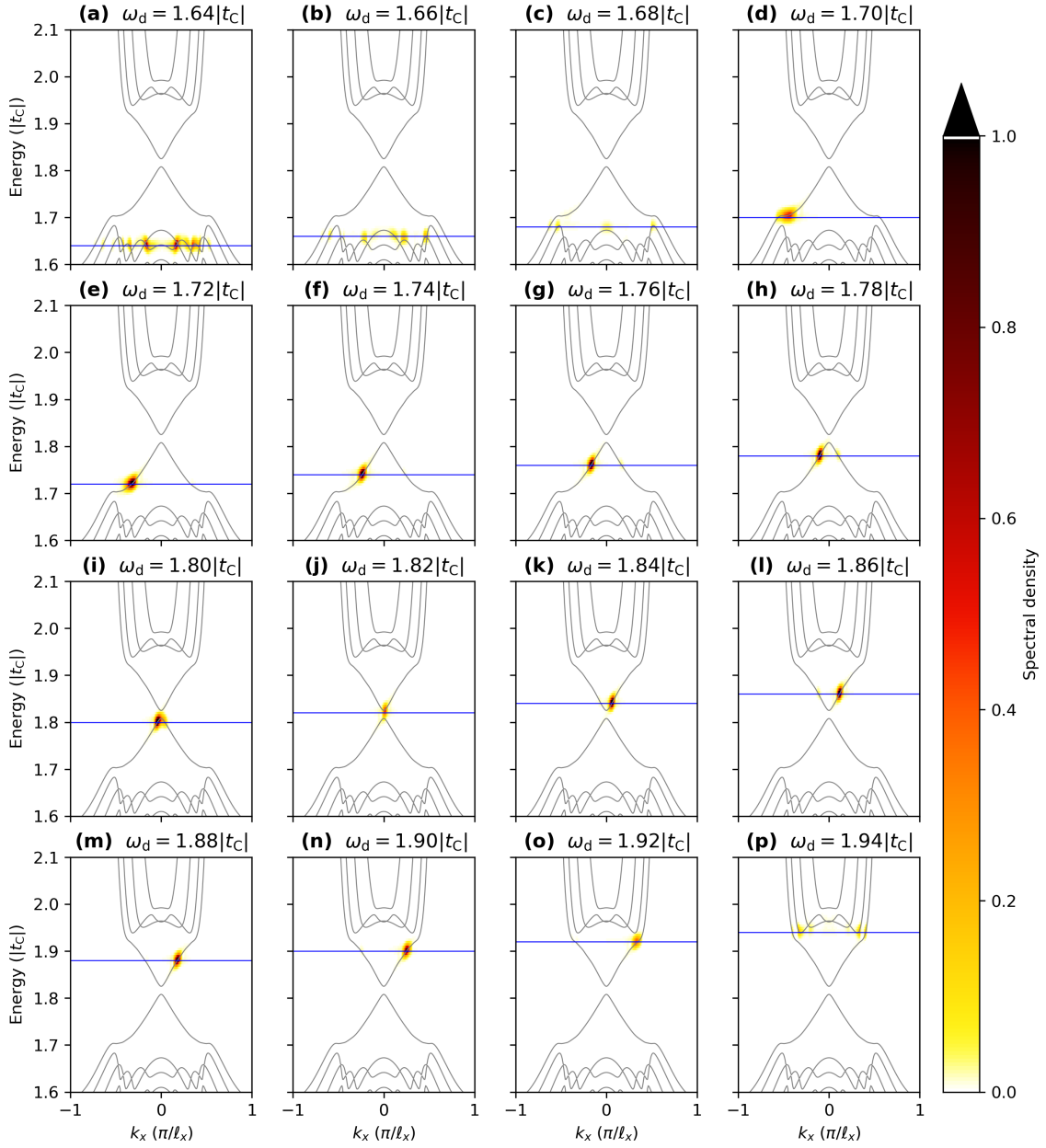


Figure 5.8 | a–p Spectral density of the driven system at a fixed probe time $t_p = 350t_{\text{hop}}$ with $\sigma_p = 100t_{\text{hop}}$ for different values of the driving frequency ω_d (blue line) in the region of the topological gap. The grey lines show the equilibrium band structure of the model. In order to improve the visibility of the edge states at a spectral resolution which does not require a substantially larger pump time, we have changed the exciton effective mass to $m_X = -10m_C$. The gap between the edge states around $\omega = 1.8|t_C|$ is a finite size effect due to the small number of y layers (compare Fig. 4.6). The other parameters are the same as in Fig. 5.7.

6 Conclusion and outlook

In this thesis, we have implemented a numerical simulation of a topological polariton model and studied its behavior under optical driving. The results presented in Sect. 5.1.2 show that it is indeed possible to optically excite the edge modes present in this system and use them for chiral transport of polariton population. We have demonstrated the robustness of this chiral transport for a simple example of an impurity in the exciton potential (Fig. 5.4) and briefly discussed the influence of exciton-exciton interaction.

In the course of our numerical studies, we have found the selective excitation of the edge mode to be difficult due to its sensitivity to changes of the driving parameters. In particular, the driving frequency needs to be tuned carefully in order to stay resonant with the edge mode without exciting the bulk. This is in part caused by the relatively small size of the topological gap. Changes to the driving protocol have also resulted in failure to selectively populate the edge mode in our simulations.

Beside the DDGPE evolution of the continuous system, we have implemented a simulation of the driven lattice model, which we have used to obtain time-resolved spectral information. The results presented in Sect. 5.2 show that the periodic driving indeed populates the bulk states at an energy corresponding to the driving frequency over the available range of lattice momenta, while within the topological gap an edge mode with definite chirality can be selectively excited.

In Sect. 3.2 we have discussed the generalization of the exciton-photon model proposed in Ref. [24] to multiple uncoupled semiconductor layers. For the special case of uniform coupling and exciton dispersion, we have seen that only a one-dimensional bright subspace is coupled to the light mode, while the rest of the excitonic eigenstates are dark. The coupling strength is enhanced by a factor proportional to \sqrt{L} . This enhancement is regularly used in experiments in order to reach high coupling strengths [1, 7]. We have found that in the uniform case the bright state retains the topological properties induced by the phase-winding coupling while the dark states are topologically trivial. In the non-interacting limit, this result is consistent with the numerical time-propagation of the multi-layer bulk model via the DDGPE (Sect. 5.1.3), where the bright state evolves in the same way as the single layer excitonic state for a rescaled coupling. This is no longer true for non-zero exciton-exciton interaction, which warrants further study on the effects of non-linearity in the multi-layer model.

The extension of this result beyond uniform coupling is still left open. Since the coupling strength varies depending on the position of the layer within the cavity in QW systems, this question might have implications for possible experimental realizations of the topological polariton model. Though probably harder to achieve in experiment, it could also be interesting to consider the effects of winding numbers differing between QW layers on the topological properties of the system. Another possible extension of this work is the incorporation of the composite nature of excitons as pairs of fermionic particles into the model, which might affect the derivation of the phase-winding exciton-photon coupling (Appendix A) and the many-body physics of the polariton system.

Qualitatively, our results are consistent with the recent experiments performed by Klemmt et al. [28], where chiral transport around a corner (compare Fig. 5.2) and the avoidance of a defect (compare Fig. 5.4) have been observed as well. With a few adaptations, our code for the trSD computation (Sect. 5.2) should be suited to obtain spectral information which can be compared to the results of the photoluminescence measurements performed by Klemmt et al. The implementation and results presented in this thesis pave the way for further studies on the selective excitation of the edge states as well as chiral transport and optical control of the polariton population, which may provide important building blocks for future polaritonic devices.

A Origin of the phase-winding exciton-photon coupling

Here we derive the form of the XC coupling term included in the model Hamiltonian (3.1), following the presentation by Karzig et al. [24].

Consider the $\mathbf{k} \cdot \mathbf{p}$ quantum well (QW) Hamiltonian

$$\hat{H}_{\text{QW}} = \sum_{\mathbf{k}} \hat{\mathbf{c}}_{\mathbf{k}}^\dagger \mathbf{H}_{\text{QW}}(\mathbf{k}) \hat{\mathbf{c}}_{\mathbf{k}} \quad (\text{A.1})$$

with spinors $\hat{\mathbf{c}}_{\mathbf{k}} := (\hat{c}_{c,\mathbf{k}}, \hat{c}_{v,\mathbf{k}})^\top$, where $\hat{c}_{c,\mathbf{k}}$ ($\hat{c}_{v,\mathbf{k}}$) is a fermionic annihilation operator for a conduction (valence) band electron¹ with momentum \mathbf{k} , and with the matrix

$$\begin{aligned} \mathbf{H}_{\text{QW}}(\mathbf{k}) &= \left(M + \frac{k^2}{2m} \right) \sigma_z + \alpha(k_x \sigma_x + k_y \sigma_y) \\ &= \begin{pmatrix} M + k^2/(2m) & \alpha(k_x - ik_y) \\ \alpha(k_x + ik_y) & -M - k^2/(2m) \end{pmatrix}. \end{aligned} \quad (\text{A.2})$$

We consider the limit of small k . This allows us to neglect the k^2 terms on the diagonal of $\mathbf{H}_{\text{QW}}(\mathbf{k})$. The Fourier transform of the current density operator has the components

$$\hat{j}_\mu(\mathbf{q}) = \sum_{\mathbf{k}} \hat{\mathbf{c}}_{\mathbf{k}+\mathbf{q}}^\dagger \mathbf{v}_\mu(\mathbf{k}) \hat{\mathbf{c}}_{\mathbf{k}}, \quad \mathbf{v}_\mu = \partial_\mu \mathbf{H}_{\text{QW}}, \quad \mu \in \{x, y\}. \quad (\text{A.3})$$

Without the diagonal terms we get \mathbf{k} -independent Pauli matrices $\mathbf{v}_\mu(\mathbf{k}) = \alpha \boldsymbol{\sigma}_\mu$ and thus obtain

$$\hat{j}_x(\mathbf{q}) = \alpha \sum_{\mathbf{k}} (\hat{c}_{c,\mathbf{k}+\mathbf{q}}^\dagger \hat{c}_{v,\mathbf{k}} + \hat{c}_{v,\mathbf{k}+\mathbf{q}}^\dagger \hat{c}_{c,\mathbf{k}}) \quad \text{and} \quad \hat{j}_y = -i\alpha \sum_{\mathbf{k}} (\hat{c}_{c,\mathbf{k}+\mathbf{q}}^\dagger \hat{c}_{v,\mathbf{k}} - \hat{c}_{v,\mathbf{k}+\mathbf{q}}^\dagger \hat{c}_{c,\mathbf{k}}). \quad (\text{A.4})$$

We can then write

$$\begin{aligned} \hat{\mathbf{j}}(\mathbf{q}) &= \sum_{\mu} \hat{j}_\mu(\mathbf{q}) \check{\mathbf{e}}_\mu \\ &= \alpha \sum_{\mathbf{k}} (\hat{c}_{c,\mathbf{k}+\mathbf{q}}^\dagger \hat{c}_{v,\mathbf{k}} + \hat{c}_{v,\mathbf{k}+\mathbf{q}}^\dagger \hat{c}_{c,\mathbf{k}}) \check{\mathbf{e}}_x + (\hat{c}_{v,\mathbf{k}+\mathbf{q}}^\dagger \hat{c}_{c,\mathbf{k}} - \hat{c}_{c,\mathbf{k}+\mathbf{q}}^\dagger \hat{c}_{v,\mathbf{k}}) i \check{\mathbf{e}}_y \\ &= \alpha \sum_{\mathbf{k}} (\check{\mathbf{e}}_x - i \check{\mathbf{e}}_y) \hat{c}_{c,\mathbf{k}+\mathbf{q}}^\dagger \hat{c}_{v,\mathbf{k}} + (\check{\mathbf{e}}_x + i \check{\mathbf{e}}_y) \hat{c}_{v,\mathbf{k}+\mathbf{q}}^\dagger \hat{c}_{c,\mathbf{k}}. \end{aligned} \quad (\text{A.5})$$

¹To be precise, \mathbf{H}_{QW} is given in the basis of $J_z = -\frac{1}{2}$ and $J_z = -\frac{3}{2}$ electron states. However, the basis transformation to the conduction and valence band operators used in the text is approximately unity for small values of k which we consider here [24].

A Origin of the phase-winding exciton-photon coupling

For equal electron and hole masses, the exciton creation operator of the lowest band (we neglect higher excitations) can be written as $\hat{a}_{X,\mathbf{q}}^\dagger = \sum_{\mathbf{k}} \phi_1(k) \hat{c}_{c,\mathbf{k}+\mathbf{q}}^\dagger \hat{c}_{v,\mathbf{k}}$ [recall (2.6)] with $\phi_1(k) = 2\sqrt{2\pi}a_0(1 + (ka_0)^2)^{-3/2} \approx 2\sqrt{2\pi}a_0$ with the exciton Bohr radius a_0 for small k . Inserting this into (A.5) yields

$$\hat{\mathbf{j}}(\mathbf{q}) = \alpha' \left[(\check{\mathbf{e}}_x - i\check{\mathbf{e}}_y) \hat{a}_{X,\mathbf{q}}^\dagger + (\check{\mathbf{e}}_x + i\check{\mathbf{e}}_y) \hat{a}_{X,-\mathbf{q}} \right] = \alpha' \left[(\check{\mathbf{e}}_x - i\check{\mathbf{e}}_y) \hat{a}_{X,\mathbf{q}}^\dagger + (\check{\mathbf{e}}_x + i\check{\mathbf{e}}_y) \hat{a}_{X,-\mathbf{q}} \right] \quad (\text{A.6})$$

with constant $\alpha' = \alpha/2\sqrt{2\pi}a_0$.

The interaction Hamiltonian is given by the coupling term [85]

$$\hat{H}_{\text{XC}} = \int d^2\mathbf{r} \hat{\mathbf{j}}(\mathbf{r}) \cdot \hat{\mathbf{A}}(\mathbf{r}) = \sum_{\mathbf{q}} \hat{\mathbf{j}}(\mathbf{q}) \cdot \hat{\mathbf{A}}(-\mathbf{q}) \quad (\text{A.7})$$

with the vector potential given by [24]

$$\hat{\mathbf{A}}(\mathbf{q}) = F_q \left(\check{\mathbf{e}}_{\perp}(\mathbf{q}) \hat{a}_{C,\mathbf{q}}^\dagger + \check{\mathbf{e}}_{\perp}(-\mathbf{q}) \hat{a}_{C,-\mathbf{q}} \right), \quad \check{\mathbf{e}}_{\perp}(\mathbf{q}) = \frac{1}{q} \begin{pmatrix} q_y \\ -q_x \end{pmatrix} \quad (\text{A.8})$$

Inserting (A.8) into (A.7) and using the rotating wave approximation (i.e., neglecting the terms proportional to $\hat{a}_X \hat{a}_C$ and $\hat{a}_X^\dagger \hat{a}_C^\dagger$) finally yields the term $\hat{H}_{\text{XC}} = \sum_{\mathbf{q}} g(\mathbf{q}) \hat{a}_{X,\mathbf{q}}^\dagger \hat{a}_{C,\mathbf{q}} + \text{H.c.}$ used in the model Hamiltonian (3.1). The interaction function is

$$g(\mathbf{q}) = -i\alpha' F_q e^{-i\theta(\mathbf{q})}. \quad (\text{A.9})$$

with the polar angle $\theta(\mathbf{q}) = \text{Arg}(q_x + iq_y) \Leftrightarrow e^{i\theta(\mathbf{q})} = \frac{1}{q}(q_x + iq_y)$.

B Computational notes

In this chapter we include two notes on computational aspects.

B.1 Simultaneous diagonalization of Hermitian matrices

Finite-dimensional Hermitian operators, such as the Hamiltonian in a numerical setting, are well known to possess an orthonormal basis of eigenstates in which they can be diagonalized. If the spectrum is simple, i.e., there are no degenerate eigenvalues, this basis is uniquely defined and all eigenstates can be labeled by their corresponding eigenvalue or, if we assume an ordering of the eigenvalues $\{\epsilon_n\}_{n=1}^N$, by the principal quantum number n . However, in the case of degenerate eigenvalues, it is no longer possible to uniquely identify an eigenstate just by knowing n . In general, one needs a *complete set of commuting observables (CSCO)*, i.e., $\mathcal{O} := \{\mathbf{O}_1, \dots, \mathbf{O}_M\}$ so that $[\mathbf{O}_i, \mathbf{O}_j] = 0$ for all $\mathbf{O}_i, \mathbf{O}_j \in \mathcal{O}$ and specifying the eigenvalues of all observables uniquely determines an eigenstate of the system. In a basis of these simultaneous eigenstates all observables in \mathcal{O} are diagonal [86].

In order to determine the band structure of a lattice Hamiltonian \mathbf{H} , as we have done in Chapter 3, it is necessary to know both energy and lattice momentum of all its eigenstates. For sufficiently small systems, the energies can be obtained by simultaneously diagonalizing both the Hamiltonian and the lattice momentum operator.

Explicitly, consider a one-dimensional periodic chain with N equally-spaced sites (we assume the distance between neighbors to be 1) and real-space basis $|j\rangle$ for $j \in [1, N]_{\mathbb{Z}}$. We can define the lattice momentum operator \mathbf{P} , which in the real-space basis has the matrix elements

$$P_{jj'} = \frac{1}{N} \sum_{m=1}^N k_m e^{-i(j-j')k_m} \quad (\text{B.1})$$

with $k_m = \frac{2\pi m}{N}$. Indeed, if \mathbf{H} is lattice-periodic, it commutes with \mathbf{P} and thus there exists a basis of simultaneous eigenstates $|n, m\rangle$ with $\mathbf{H}|n, m\rangle = \epsilon_n|n, m\rangle$ and $\mathbf{P}|n, m\rangle = k_m|n, m\rangle$ where n labels the *distinct* energy levels of the system. If this basis is known, it contains all information on the band structure of the system. However, the eigenbasis obtained by numerically diagonalizing \mathbf{H} (or \mathbf{P}) alone is not necessarily a simultaneous eigenbasis.

One way to obtain both quantum numbers is to analytically determine the \mathbf{P} -invariant blocks $\mathbf{h}(k_m)$ of \mathbf{H} , so that $\mathbf{H} \sim \bigoplus_{m=1}^N \mathbf{h}(k_m)$, and then diagonalize each $\mathbf{h}(k_m)$ separately. In cases where this can be done, this approach is preferable both for its reduced computational cost and the fact that the diagonalization of each block can be performed in parallel. We have used this approach, e.g., in Sects. 4.2 and 4.3.

It is also possible to perform the simultaneous diagonalization numerically, which can be useful, e.g., to cross-check the results of an analytic calculation. One solution is to first diagonalize \mathbf{H} numerically and transform \mathbf{P} to the obtained eigenbasis. Generally, this will yield a block-diagonal matrix and it is then possible to diagonalize each block. This method of successive diagonalization is, however, unstable in the presence of numerical noise [87] and can be tedious to implement. A surprisingly simple alternative is to instead randomly choose a parameter $\lambda \in (0, 1)$ and compute the eigenbasis of the linear combination

$$\mathbf{L} = \mathbf{H} + \lambda \mathbf{P}. \quad (\text{B.2})$$

In practice, both \mathbf{H} and \mathbf{P} tend to be diagonal in this basis. More generally, in order to compute the simultaneous eigenbasis of the set of operators \mathcal{O} , one can diagonalize the so-called matrix pencil

$$\mathbf{L} = \sum_{i=1}^M \lambda^{i-1} \mathbf{O}_i. \quad (\text{B.3})$$

While we are not aware of a rigorous proof of the properties of this approach, its feasibility seems to be related to the fact that randomly generated Hermitian matrices have a simple spectrum with high probability (see, e.g., Tao and Vu [88, Theorem 5]), so that the random linear combination of Eqs. (B.2) and (B.3) tends to lift all degeneracies.

B.2 Discretizing the Fourier transform

Consider the field $\psi: \mathbb{R}^d \rightarrow \mathbb{C}$ which is discretized over the cuboid $\mathcal{V} := \prod_{\mu=1}^d [0, L_\mu]$ at points $\mathbf{x}[\mathbf{j}] := (j_1 \ell_1, \dots, j_d \ell_d) \in \mathbb{R}^d$ where ℓ_μ is the discretization length in μ direction and with the indices $\mathbf{j} = (j_1, \dots, j_d) \in \mathcal{J} := J_1 \times \dots \times J_d$ with $J_\mu := [0, N_\mu - 1]_{\mathbb{Z}}$ and $N_\mu := \frac{L_\mu}{\ell_\mu} \in \mathbb{N}_+$.

The Fourier transform of $\psi(\mathbf{x})$ can be approximated by a Riemann sum as

$$\tilde{\psi}(\mathbf{q}) = \int_{\mathcal{V}} d^d \mathbf{x} \psi(\mathbf{x}) e^{-i\mathbf{q} \cdot \mathbf{x}} \approx \delta_V \sum_{\mathbf{j} \in \mathcal{J}} \psi[\mathbf{j}] e^{-i\mathbf{q} \cdot \mathbf{x}[\mathbf{j}]} \quad (\text{B.4})$$

where $\psi[\mathbf{j}] := \psi(\mathbf{x}[\mathbf{j}])$ and $\delta_V := \ell_1 \dots \ell_d$. Discretizing the Fourier space as

$$\mathbf{q}[\mathbf{k}] := 2\pi \left(\frac{k_1}{L_1}, \dots, \frac{k_d}{L_d} \right) \text{ where } \mathbf{k} \in \mathcal{J}, \quad (\text{B.5})$$

we get, using $\zeta_N := e^{i2\pi/N}$,

$$\begin{aligned}
 \tilde{\psi}(\mathbf{q}[\mathbf{k}]) &\approx \delta_V \sum_{\mathbf{j} \in \mathcal{J}} \psi[\mathbf{j}] e^{-i\mathbf{q}[\mathbf{k}] \cdot \mathbf{x}[\mathbf{j}]} \\
 &= \delta_V \sum_{\mathbf{j} \in \mathcal{J}} \psi[\mathbf{j}] e^{-i \sum_{\mu=1}^d \frac{2\pi k_\mu}{L_\mu} j_\mu \ell_\mu} \\
 &= \delta_V \sum_{\mathbf{j} \in \mathcal{J}} \psi[\mathbf{j}] e^{-i \sum_{\mu=1}^d \frac{j_\mu k_\mu}{N_\mu}} \tag{B.6} \\
 &= \delta_V \sum_{j_1=0}^{N_1-1} \cdots \sum_{j_d=0}^{N_d-1} \psi[\mathbf{j}] \zeta_{N_1}^{-k_1 j_1} \cdots \zeta_{N_d}^{-k_d j_d} \\
 &= \delta_V \text{DFT}_d(\boldsymbol{\psi})[\mathbf{k}].
 \end{aligned}$$

which is, up to the prefactor, the d -dimensional discrete Fourier transform (DFT) of the array $\boldsymbol{\psi} := \{\psi[\mathbf{j}]\}_{\mathbf{j} \in \mathcal{J}}$, which can be directly evaluated using the FFT [75, 78].

Bibliography

- [1] Michael Ruggenthaler, Nicolas Tancogne-Dejean, Johannes Flick, Heiko Appel, and Angel Rubio. “From a quantum-electrodynamical light–matter description to novel spectroscopies”. In: *Nature Reviews Chemistry* 2.3 (Mar. 2018), p. 0118. ISSN: 2397-3358. DOI: [10.1038/s41570-018-0118](https://doi.org/10.1038/s41570-018-0118) (cit. on pp. 11, 57).
- [2] Michele Buzzi, Michael Först, Roman Mankowsky, and Andrea Cavalleri. “Probing dynamics in quantum materials with femtosecond X-rays”. In: *Nature Reviews Materials* 3.9 (Sept. 2018), p. 299. ISSN: 2058-8437. DOI: [10.1038/s41578-018-0024-9](https://doi.org/10.1038/s41578-018-0024-9) (cit. on p. 11).
- [3] Netanel H. Lindner, Gil Refael, and Victor Galitski. “Floquet topological insulator in semiconductor quantum wells”. In: *Nature Physics* 7.6 (June 2011), pp. 490–495. ISSN: 1745-2473, 1745-2481. DOI: [10.1038/nphys1926](https://doi.org/10.1038/nphys1926) (cit. on pp. 11, 24, 25).
- [4] Hannes Hübener, Michael A. Sentef, Umberto De Giovannini, Alexander F. Kemper, and Angel Rubio. “Creating stable Floquet–Weyl semimetals by laser-driving of 3D Dirac materials”. In: *Nature Communications* 8 (Jan. 17, 2017), p. 13940. ISSN: 2041-1723. DOI: [10.1038/ncomms13940](https://doi.org/10.1038/ncomms13940) (cit. on p. 11).
- [5] Vincenzo Savona, Carlo Piermarocchi, Antonio Quattropani, Paolo Schwendimann, and Francesco Tassone. “Optical properties of microcavity polaritons”. In: *Phase Transitions* 68.1 (Feb. 1999), pp. 169–279. ISSN: 0141-1594, 1029-0338. DOI: [10.1080/01411599908224518](https://doi.org/10.1080/01411599908224518) (cit. on pp. 11, 13, 15).
- [6] J. J. Hopfield and D. G. Thomas. “Polariton Absorption Lines”. In: *Physical Review Letters* 15.1 (July 5, 1965), pp. 22–25. DOI: [10.1103/PhysRevLett.15.22](https://doi.org/10.1103/PhysRevLett.15.22) (cit. on p. 11).
- [7] Iacopo Carusotto and Cristiano Ciuti. “Quantum fluids of light”. In: *Reviews of Modern Physics* 85.1 (Feb. 21, 2013), pp. 299–366. DOI: [10.1103/RevModPhys.85.299](https://doi.org/10.1103/RevModPhys.85.299) (cit. on pp. 11, 14, 24, 45, 57).
- [8] J. Kasprzak, M. Richard, S. Kundermann, A. Baas, P. Jeambrun, J. M. J. Keeling, F. M. Marchetti, M. H. Szymańska, R. André, J. L. Staehli, V. Savona, P. B. Littlewood, B. Deveaud, and Le Si Dang. “Bose–Einstein condensation of exciton polaritons”. In: *Nature* 443.7110 (Sept. 2006), pp. 409–414. ISSN: 1476-4687. DOI: [10.1038/nature05131](https://doi.org/10.1038/nature05131) (cit. on p. 11).

Bibliography

- [9] Hui Deng, Hartmut Haug, and Yoshihisa Yamamoto. “Exciton-polariton Bose-Einstein condensation”. In: *Reviews of Modern Physics* 82.2 (May 12, 2010), pp. 1489–1537. ISSN: 0034-6861, 1539-0756. DOI: [10.1103/RevModPhys.82.1489](https://doi.org/10.1103/RevModPhys.82.1489) (cit. on pp. 11, 13–16, 24).
- [10] Tim Byrnes, Na Young Kim, and Yoshihisa Yamamoto. “Exciton-polariton condensates”. In: *Nature Physics* 10.11 (Oct. 31, 2014), pp. 803–813. ISSN: 1745-2473, 1745-2481. DOI: [10.1038/nphys3143](https://doi.org/10.1038/nphys3143) (cit. on pp. 11, 13, 14).
- [11] K. G. Lagoudakis, M. Wouters, M. Richard, A. Baas, I. Carusotto, R. André, Le Si Dang, and B. Deveaud-Plédran. “Quantized vortices in an exciton-polariton condensate”. In: *Nature Physics* 4.9 (Sept. 2008), pp. 706–710. ISSN: 1745-2481. DOI: [10.1038/nphys1051](https://doi.org/10.1038/nphys1051) (cit. on p. 11).
- [12] M. Romanelli, C. Leyder, J. Ph. Karr, E. Giacobino, and A. Bramati. “Four Wave Mixing Oscillation in a Semiconductor Microcavity: Generation of Two Correlated Polariton Populations”. In: *Physical Review Letters* 98.10 (Mar. 7, 2007), p. 106401. DOI: [10.1103/PhysRevLett.98.106401](https://doi.org/10.1103/PhysRevLett.98.106401) (cit. on p. 11).
- [13] M. Sich, D. N. Krizhanovskii, M. S. Skolnick, A. V. Gorbach, R. Hartley, D. V. Skryabin, E. A. Cerda-Méndez, K. Biermann, R. Hey, and P. V. Santos. “Observation of bright polariton solitons in a semiconductor microcavity”. In: *Nature Photonics* 6.1 (Jan. 2012), pp. 50–55. ISSN: 1749-4893. DOI: [10.1038/nphoton.2011.267](https://doi.org/10.1038/nphoton.2011.267) (cit. on p. 11).
- [14] G. Grosso, G. Nardin, F. Morier-Genoud, Y. Léger, and B. Deveaud-Plédran. “Dynamics of dark-soliton formation in a polariton quantum fluid”. In: *Physical Review B* 86.2 (July 30, 2012), p. 020509. DOI: [10.1103/PhysRevB.86.020509](https://doi.org/10.1103/PhysRevB.86.020509) (cit. on p. 11).
- [15] Immanuel Bloch, Jean Dalibard, and Wilhelm Zwerger. “Many-body physics with ultracold gases”. In: *Reviews of Modern Physics* 80.3 (July 18, 2008), pp. 885–964. DOI: [10.1103/RevModPhys.80.885](https://doi.org/10.1103/RevModPhys.80.885) (cit. on pp. 11, 45).
- [16] D. Ballarini, M. De Giorgi, E. Cancellieri, R. Houdré, E. Giacobino, R. Cingolani, A. Bramati, G. Gigli, and D. Sanvitto. “All-optical polariton transistor”. In: *Nature Communications* 4 (Apr. 30, 2013), p. 1778. ISSN: 2041-1723. DOI: [10.1038/ncomms2734](https://doi.org/10.1038/ncomms2734) (cit. on pp. 11, 46).
- [17] Félix Marsault, Hai Son Nguyen, Dimitrii Tanese, Aristide Lemaître, Elisabeth Galopin, Isabelle Sagnes, Alberto Amo, and Jacqueline Bloch. “Realization of an all optical exciton-polariton router”. In: *Applied Physics Letters* 107.20 (Nov. 16, 2015), p. 201115. ISSN: 0003-6951. DOI: [10.1063/1.4936158](https://doi.org/10.1063/1.4936158) (cit. on p. 11).
- [18] Daniele Sanvitto and Stéphane Kéna-Cohen. “The road towards polaritonic devices”. In: *Nature Materials* 15.10 (Oct. 2016), pp. 1061–1073. ISSN: 1476-4660. DOI: [10.1038/nmat4668](https://doi.org/10.1038/nmat4668) (cit. on pp. 11, 16).

- [19] B. Andrei Bernevig. *Topological Insulators and Topological Superconductors*. Course Book. Berlin, Boston: Princeton University Press, 2013. ISBN: 978-1-4008-4673-3. DOI: [10.1515/9781400846733](https://doi.org/10.1515/9781400846733) (cit. on p. 11).
- [20] János K. Asbóth, László Oroszlány, and András Pályi. *A short course on topological insulators: band structure and edge states in one and two dimensions*. Lecture notes in physics volume 919. OCLC: 942849465. Cham Heidelberg New York Dordrecht London: Springer, 2016. 166 pp. ISBN: 978-3-319-25607-8 (cit. on pp. 11, 35, 38).
- [21] L. Fritz and A. Altland. “Topology in condensed matter”. In: *Topological Matter: Topological Insulators, Skyrmions and Majoranas*. Vol. 139. Schriften des Forschungszentrums Jülich, Reihe Schlüsseltechnologien. Mar. 2017. ISBN: 978-3-95806-202-3 (cit. on pp. 11, 16, 19).
- [22] F. D. M. Haldane and S. Raghu. “Possible Realization of Directional Optical Waveguides in Photonic Crystals with Broken Time-Reversal Symmetry”. In: *Physical Review Letters* 100.1 (Jan. 10, 2008). ISSN: 0031-9007, 1079-7114. DOI: [10.1103/PhysRevLett.100.013904](https://doi.org/10.1103/PhysRevLett.100.013904) (cit. on p. 11).
- [23] S. Raghu and F. D. M. Haldane. “Analogues of quantum-Hall-effect edge states in photonic crystals”. In: *Physical Review A* 78.3 (Sept. 23, 2008). ISSN: 1050-2947, 1094-1622. DOI: [10.1103/PhysRevA.78.033834](https://doi.org/10.1103/PhysRevA.78.033834) (cit. on p. 11).
- [24] Torsten Karzig, Charles-Edouard Bardyn, Netanel H. Lindner, and Gil Refael. “Topological Polaritons”. In: *Physical Review X* 5.3 (July 1, 2015), p. 031001. DOI: [10.1103/PhysRevX.5.031001](https://doi.org/10.1103/PhysRevX.5.031001) (cit. on pp. 11, 12, 23, 24, 27, 46, 48, 57, 59, 60).
- [25] A. V. Nalitov, D. D. Solnyshkov, and G. Malpuech. “Polariton \mathbb{Z} Topological Insulator”. In: *Physical Review Letters* 114.11 (Mar. 16, 2015), p. 116401. DOI: [10.1103/PhysRevLett.114.116401](https://doi.org/10.1103/PhysRevLett.114.116401) (cit. on pp. 11, 12).
- [26] Charles-Edouard Bardyn, Torsten Karzig, Gil Refael, and Timothy C. H. Liew. “Topological polaritons and excitons in garden-variety systems”. In: *Physical Review B* 91.16 (Apr. 29, 2015), p. 161413. DOI: [10.1103/PhysRevB.91.161413](https://doi.org/10.1103/PhysRevB.91.161413) (cit. on pp. 11, 12).
- [27] V. Peano, C. Brendel, M. Schmidt, and F. Marquardt. “Topological Phases of Sound and Light”. In: *Physical Review X* 5.3 (July 28, 2015), p. 031011. DOI: [10.1103/PhysRevX.5.031011](https://doi.org/10.1103/PhysRevX.5.031011) (cit. on p. 11).
- [28] S. Klemmt, T. H. Harder, O. A. Egorov, K. Winkler, R. Ge, M. A. Bandres, M. Emmerling, L. Worschech, T. C. H. Liew, M. Segev, C. Schneider, and S. Höfling. “Exciton-polariton topological insulator”. In: *Nature* 562.7728 (Oct. 2018), p. 552. ISSN: 1476-4687. DOI: [10.1038/s41586-018-0601-5](https://doi.org/10.1038/s41586-018-0601-5) (cit. on pp. 12, 58).
- [29] Monique Combescot and Shiue-Yuan Shiau. *Excitons and cooper pairs: two composite bosons in many-body physics*. 1st edition. New York, NY: Oxford University Press, 2015. ISBN: 978-0-19-875373-5 (cit. on pp. 14, 15, 24).

Bibliography

- [30] D. J. Thouless, M. Kohmoto, M. P. Nightingale, and M. den Nijs. “Quantized Hall Conductance in a Two-Dimensional Periodic Potential”. In: *Physical Review Letters* 49.6 (Aug. 9, 1982), pp. 405–408. DOI: [10.1103/PhysRevLett.49.405](https://doi.org/10.1103/PhysRevLett.49.405) (cit. on pp. 16, 18).
- [31] Di Xiao, Ming-Che Chang, and Qian Niu. “Berry phase effects on electronic properties”. In: *Reviews of Modern Physics* 82.3 (July 6, 2010), pp. 1959–2007. ISSN: 0034-6861, 1539-0756. DOI: [10.1103/RevModPhys.82.1959](https://doi.org/10.1103/RevModPhys.82.1959) (cit. on pp. 16, 20).
- [32] M. V. Berry. “Quantal Phase Factors Accompanying Adiabatic Changes”. In: *Proceedings of the Royal Society A: Mathematical, Physical and Engineering Sciences* 392.1802 (Mar. 8, 1984), pp. 45–57. ISSN: 1364-5021, 1471-2946. DOI: [10.1098/rspa.1984.0023](https://doi.org/10.1098/rspa.1984.0023) (cit. on pp. 16, 17).
- [33] Jean Dalibard, Fabrice Gerbier, Gediminas Juzeliūnas, and Patrik Öhberg. “Colloquium: Artificial gauge potentials for neutral atoms”. In: *Reviews of Modern Physics* 83.4 (Nov. 30, 2011), pp. 1523–1543. ISSN: 0034-6861, 1539-0756. DOI: [10.1103/RevModPhys.83.1523](https://doi.org/10.1103/RevModPhys.83.1523) (cit. on pp. 16, 18).
- [34] Jean Dalibard. *Introduction to the physics of artificial gauge fields*. 2015. eprint: [arXiv : 1504.05520](https://arxiv.org/abs/1504.05520) (cit. on pp. 16, 18).
- [35] Monika Aidelsburger. “Artificial gauge fields with ultracold atoms in optical lattices”. PhD thesis. Feb. 2015. URL: <http://nbn-resolving.de/urn:nbn:de:bvb:19-181480> (cit. on pp. 16, 21).
- [36] N. Goldman, J. C. Budich, and P. Zoller. “Topological quantum matter with ultracold gases in optical lattices”. In: *Nature Physics* 12.7 (July 2016), pp. 639–645. ISSN: 1745-2481. DOI: [10.1038/nphys3803](https://doi.org/10.1038/nphys3803) (cit. on pp. 16, 18).
- [37] Naoto Nagaosa and Yoshinori Tokura. “Topological properties and dynamics of magnetic skyrmions”. In: *Nature Nanotechnology* 8.12 (Dec. 4, 2013), pp. 899–911. ISSN: 1748-3387, 1748-3395. DOI: [10.1038/nnano.2013.243](https://doi.org/10.1038/nnano.2013.243) (cit. on pp. 16, 27).
- [38] Mikio Nakahara. *Differentialgeometrie, Topologie und Physik*. Berlin, Heidelberg: Springer, 2015. ISBN: 978-3-662-45299-8. DOI: [10.1007/978-3-662-45300-1](https://doi.org/10.1007/978-3-662-45300-1) (cit. on pp. 16, 18).
- [39] M. Born and V. Fock. “Beweis des Adiabatsensatzes”. In: *Zeitschrift für Physik* 51.3 (Mar. 1928), pp. 165–180. ISSN: 1434-6001, 1434-601X. DOI: [10.1007/BF01343193](https://doi.org/10.1007/BF01343193) (cit. on p. 17).
- [40] Tosio Kato. “On the Adiabatic Theorem of Quantum Mechanics”. In: *Journal of the Physical Society of Japan* 5.6 (Nov. 15, 1950), pp. 435–439. ISSN: 0031-9015. DOI: [10.1143/JPSJ.5.435](https://doi.org/10.1143/JPSJ.5.435) (cit. on p. 17).
- [41] Barry Simon. “Holonomy, the Quantum Adiabatic Theorem, and Berry’s Phase”. In: *Physical Review Letters* 51.24 (Dec. 12, 1983), pp. 2167–2170. DOI: [10.1103/PhysRevLett.51.2167](https://doi.org/10.1103/PhysRevLett.51.2167) (cit. on p. 18).

- [42] Y. Aharonov and D. Bohm. “Significance of Electromagnetic Potentials in the Quantum Theory”. In: *Physical Review* 115.3 (Aug. 1, 1959), pp. 485–491. DOI: [10.1103/PhysRev.115.485](https://doi.org/10.1103/PhysRev.115.485) (cit. on p. 18).
- [43] Frank Wilczek and A. Zee. “Appearance of gauge structure in simple dynamical systems”. In: *Physical Review Letters* 52.24 (1984), p. 2111 (cit. on pp. 18, 21).
- [44] M. Z. Hasan and C. L. Kane. “Colloquium: Topological insulators”. In: *Reviews of Modern Physics* 82.4 (Nov. 8, 2010), pp. 3045–3067. DOI: [10.1103/RevModPhys.82.3045](https://doi.org/10.1103/RevModPhys.82.3045) (cit. on p. 18).
- [45] K. v. Klitzing, G. Dorda, and M. Pepper. “New Method for High-Accuracy Determination of the Fine-Structure Constant Based on Quantized Hall Resistance”. In: *Physical Review Letters* 45.6 (Aug. 11, 1980), pp. 494–497. DOI: [10.1103/PhysRevLett.45.494](https://doi.org/10.1103/PhysRevLett.45.494) (cit. on p. 18).
- [46] Mahito Kohmoto. “Topological invariant and the quantization of the Hall conductance”. In: *Annals of Physics* 160.2 (Apr. 1, 1985), pp. 343–354. ISSN: 0003-4916. DOI: [10.1016/0003-4916\(85\)90148-4](https://doi.org/10.1016/0003-4916(85)90148-4) (cit. on pp. 18, 19).
- [47] Yasuhiro Hatsugai. “Chern number and edge states in the integer quantum Hall effect”. In: *Physical Review Letters* 71.22 (Nov. 29, 1993), pp. 3697–3700. DOI: [10.1103/PhysRevLett.71.3697](https://doi.org/10.1103/PhysRevLett.71.3697) (cit. on p. 19).
- [48] Andrew M. Essin and Victor Gurarie. “Bulk-boundary correspondence of topological insulators from their respective Green’s functions”. In: *Physical Review B* 84.12 (Sept. 28, 2011), p. 125132. DOI: [10.1103/PhysRevB.84.125132](https://doi.org/10.1103/PhysRevB.84.125132) (cit. on p. 19).
- [49] Andreas P. Schnyder, Shinsei Ryu, Akira Furusaki, and Andreas W. W. Ludwig. “Classification of topological insulators and superconductors in three spatial dimensions”. In: *Physical Review B* 78.19 (Nov. 26, 2008), p. 195125. DOI: [10.1103/PhysRevB.78.195125](https://doi.org/10.1103/PhysRevB.78.195125) (cit. on p. 19).
- [50] Andreas P. Schnyder, Shinsei Ryu, Akira Furusaki, and Andreas W. W. Ludwig. “Classification of Topological Insulators and Superconductors”. In: *AIP Conference Proceedings* 1134.1 (May 14, 2009), pp. 10–21. ISSN: 0094-243X. DOI: [10.1063/1.3149481](https://doi.org/10.1063/1.3149481) (cit. on p. 19).
- [51] Alexei Kitaev. “Periodic table for topological insulators and superconductors”. In: *AIP Conference Proceedings* 1134.1 (May 14, 2009), pp. 22–30. ISSN: 0094-243X. DOI: [10.1063/1.3149495](https://doi.org/10.1063/1.3149495) (cit. on p. 19).
- [52] Shinsei Ryu, Andreas P. Schnyder, Akira Furusaki, and Andreas W. W. Ludwig. “Topological insulators and superconductors: tenfold way and dimensional hierarchy”. In: *New Journal of Physics* 12.6 (2010), p. 065010. ISSN: 1367-2630. DOI: [10.1088/1367-2630/12/6/065010](https://doi.org/10.1088/1367-2630/12/6/065010) (cit. on p. 19).

Bibliography

- [53] Takahiro Fukui, Yasuhiro Hatsugai, and Hiroshi Suzuki. “Chern Numbers in Discretized Brillouin Zone: Efficient Method of Computing (Spin) Hall Conductances”. In: *Journal of the Physical Society of Japan* 74.6 (June 15, 2005), pp. 1674–1677. ISSN: 0031-9015, 1347-4073. DOI: [10.1143/JPSJ.74.1674](https://doi.org/10.1143/JPSJ.74.1674) (cit. on pp. 20, 21).
- [54] J. Bezanson, A. Edelman, S. Karpinski, and V. Shah. “Julia: A Fresh Approach to Numerical Computing”. In: *SIAM Review* 59.1 (Jan. 1, 2017), pp. 65–98. ISSN: 0036-1445. DOI: [10.1137/141000671](https://doi.org/10.1137/141000671) (cit. on p. 22).
- [55] G. Tkachov. “Topology from model Hamiltonians”. In: *Topological Matter: Topological Insulators, Skyrmions and Majoranas*. Vol. 139. Schriften des Forschungszentrums Jülich, Reihe Schlüsseltechnologien. Mar. 2017. ISBN: 978-3-95806-202-3 (cit. on p. 25).
- [56] Karin Everschor-Sitte and Matthias Sitte. *File:2skyrmions.PNG — Wikimedia Commons, the free media repository*. 2017. URL: <https://commons.wikimedia.org/w/index.php?title=File:2skyrmions.PNG&oldid=262950254> (visited on 2018-10-16) (cit. on p. 25).
- [57] *Creative Commons Attribution-ShareAlike 3.0 Unported*. Creative Commons. URL: <https://creativecommons.org/licenses/by-sa/3.0/> (visited on 2018-10-16) (cit. on p. 25).
- [58] D.P O’Leary and G.W Stewart. “Computing the eigenvalues and eigenvectors of symmetric arrowhead matrices”. In: *Journal of Computational Physics* 90.2 (1990), pp. 497–505. ISSN: 0021-9991. DOI: [10.1016/0021-9991\(90\)90177-3](https://doi.org/10.1016/0021-9991(90)90177-3) (cit. on p. 29).
- [59] Suk-Geun Hwang. “Cauchy’s interlace theorem for eigenvalues of Hermitian matrices”. In: *American Mathematical Monthly* (2004), pp. 157–159 (cit. on p. 29).
- [60] Peter Lambropoulos and David Petrosyan. *Fundamentals of quantum optics and quantum information*. OCLC: 316064238. Berlin: Springer, 2007. ISBN: 978-3-540-34572-5. URL: <http://dx.doi.org/10.1007/978-3-540-34572-5> (visited on 2018-09-14) (cit. on p. 30).
- [61] Raphael F. Ribeiro, Luis A. Martínez-Martínez, Matthew Du, Jorge Campos-Gonzalez-Angulo, and Joel Yuen-Zhou. “Polariton chemistry: controlling molecular dynamics with optical cavities”. In: *Chemical Science* 9.30 (Aug. 1, 2018), pp. 6325–6339. ISSN: 2041-6539. DOI: [10.1039/C8SC01043A](https://doi.org/10.1039/C8SC01043A) (cit. on p. 30).
- [62] Philip A. Vetter, LuoJia Wang, Da-Wei Wang, and Marlan O. Scully. “Single photon subradiance and superradiance revisited: a group theoretic analysis of subradiant states”. In: *Physica Scripta* 91.2 (2016), p. 023007. ISSN: 1402-4896. DOI: [10.1088/0031-8949/91/2/023007](https://doi.org/10.1088/0031-8949/91/2/023007) (cit. on p. 30).
- [63] Xiao-Liang Qi, Yong-Shi Wu, and Shou-Cheng Zhang. “Topological quantization of the spin Hall effect in two-dimensional paramagnetic semiconductors”. In: *Physical Review B* 74.8 (Aug. 10, 2006), p. 085308. DOI: [10.1103/PhysRevB.74.085308](https://doi.org/10.1103/PhysRevB.74.085308) (cit. on p. 35).

- [64] B. Andrei Bernevig, Taylor L. Hughes, and Shou-Cheng Zhang. “Quantum Spin Hall Effect and Topological Phase Transition in HgTe Quantum Wells”. In: *Science* 314.5806 (Dec. 15, 2006), pp. 1757–1761. ISSN: 0036-8075, 1095-9203. DOI: [10.1126/science.1133734](https://doi.org/10.1126/science.1133734) (cit. on p. 35).
- [65] Talitha Weiß. “Nonlinear dynamics in quantum synchronization and topological transport”. PhD thesis. Friedrich-Alexander-Universität Erlangen-Nürnberg, 2017. URL: http://theorie2.physik.uni-erlangen.de/images/3/3e/2017_Weiss_PhDThesis.pdf (visited on 2018-10-19) (cit. on p. 35).
- [66] A. Pertsova, C. M. Canali, and A. H. MacDonald. “Quantum Hall edge states in topological insulator nanoribbons”. In: *Physical Review B* 94.12 (Sept. 26, 2016), p. 121409. DOI: [10.1103/PhysRevB.94.121409](https://doi.org/10.1103/PhysRevB.94.121409) (cit. on p. 39).
- [67] Gianluca Stefanucci and Robert van Leeuwen. *Nonequilibrium many-body theory of quantum systems: a modern introduction*. Cambridge: Cambridge University Press, 2013. 600 pp. ISBN: 978-0-521-76617-3 (cit. on pp. 42, 43).
- [68] Marlan O. Scully and Muhammad Suhail Zubairy. *Quantum optics*. Cambridge University Press, 1997. 630 pp. ISBN: 978-0-521-43458-4 (cit. on p. 43).
- [69] C. C. Gerry and Peter Knight. *Introductory quantum optics*. Cambridge, UK ; New York: Cambridge University Press, 2005. 317 pp. ISBN: 978-0-521-82035-6 (cit. on p. 43).
- [70] Christian Weedbrook, Stefano Pirandola, Raúl García-Patrón, Nicolas J. Cerf, Timothy C. Ralph, Jeffrey H. Shapiro, and Seth Lloyd. “Gaussian quantum information”. In: *Reviews of Modern Physics* 84.2 (May 1, 2012), pp. 621–669. DOI: [10.1103/RevModPhys.84.621](https://doi.org/10.1103/RevModPhys.84.621) (cit. on p. 44).
- [71] Tao Shi, Eugene Demler, and J. Ignacio Cirac. “Variational study of fermionic and bosonic systems with non-Gaussian states: Theory and applications”. In: *Annals of Physics* 390 (Mar. 1, 2018), pp. 245–302. ISSN: 0003-4916. DOI: [10.1016/j.aop.2017.11.014](https://doi.org/10.1016/j.aop.2017.11.014) (cit. on p. 44).
- [72] Adrian Stan, Nils Erik Dahlen, and Robert van Leeuwen. “Time propagation of the Kadanoff–Baym equations for inhomogeneous systems”. In: *The Journal of Chemical Physics* 130.22 (June 9, 2009), p. 224101. ISSN: 0021-9606. DOI: [10.1063/1.3127247](https://doi.org/10.1063/1.3127247) (cit. on p. 44).
- [73] A. J. Leggett. *Quantum liquids: Bose condensation and Cooper pairing in condensed-matter systems*. Oxford graduate texts. OCLC: ocm74710721. Oxford ; New York: Oxford University Press, 2006. 388 pp. ISBN: 978-0-19-852643-8 (cit. on p. 45).
- [74] L. P Pitaevskii and S Stringari. *Bose-Einstein condensation and superfluidity*. OCLC: 936040211. 2016. ISBN: 978-0-19-107668-8. (Visited on 2018-09-19) (cit. on pp. 45, 46).
- [75] M. Frigo and S.G. Johnson. “The Design and Implementation of FFTW3”. In: *Proceedings of the IEEE* 93.2 (Feb. 2005), pp. 216–231. ISSN: 0018-9219. DOI: [10.1109/JPROC.2004.840301](https://doi.org/10.1109/JPROC.2004.840301) (cit. on pp. 46, 63).

Bibliography

- [76] J.R. Dormand and P.J. Prince. “A family of embedded Runge-Kutta formulae”. In: *Journal of Computational and Applied Mathematics* 6.1 (Mar. 1980), pp. 19–26. ISSN: 03770427. DOI: [10.1016/0771-050X\(80\)90013-3](https://doi.org/10.1016/0771-050X(80)90013-3) (cit. on p. 47).
- [77] Karsten Ahnert and Mario Mulansky. “Odeint – Solving Ordinary Differential Equations in C++”. In: *AIP Conference Proceedings* 1389.1 (2011), pp. 1586–1589. DOI: [10.1063/1.3637934](https://doi.org/10.1063/1.3637934) (cit. on p. 47).
- [78] William H. Press, ed. *Numerical recipes: the art of scientific computing*. 3rd ed. OCLC: ocn123285342. Cambridge, UK ; New York: Cambridge University Press, 2007. 1235 pp. ISBN: 978-0-521-88068-8 (cit. on pp. 47, 63).
- [79] Russ Rew, Glenn Davis, Steve Emmerson, Cathy Cormack, John Caron, Robert Pincus, Ed Hartnett, Dennis Heimbigner, Lynton Appel, and Ward Fisher. *Unidata NetCDF*. DOI: [10.5065/D6H70CW6](https://doi.org/10.5065/D6H70CW6) (cit. on p. 48).
- [80] S. Hoyer and J. Hamman. “xarray: N-D labeled arrays and datasets in Python”. In: *Journal of Open Research Software* 5.1 (2017). DOI: [10.5334/jors.148](https://doi.org/10.5334/jors.148) (cit. on p. 48).
- [81] Dask Development Team. *Dask: Library for dynamic task scheduling*. 2016. URL: <http://dask.pydata.org> (cit. on p. 48).
- [82] J. D. Hunter. “Matplotlib: A 2D graphics environment”. In: *Computing In Science & Engineering* 9.3 (2007), pp. 90–95. DOI: [10.1109/MCSE.2007.55](https://doi.org/10.1109/MCSE.2007.55) (cit. on p. 48).
- [83] Ole Tange. *GNU Parallel 2018*. Mar. 2018. DOI: [10.5281/zenodo.1146014](https://doi.org/10.5281/zenodo.1146014) (cit. on p. 48).
- [84] J. K. Freericks, H. R. Krishnamurthy, and Th. Pruschke. “Theoretical Description of Time-Resolved Photoemission Spectroscopy: Application to Pump-Probe Experiments”. In: *Physical Review Letters* 102.13 (Mar. 30, 2009), p. 136401. DOI: [10.1103/PhysRevLett.102.136401](https://doi.org/10.1103/PhysRevLett.102.136401) (cit. on p. 54).
- [85] Walter Greiner and Joachim Reinhardt. *Field Quantization*. Berlin, Heidelberg: Springer Berlin Heidelberg, 1996. ISBN: 978-3-540-78048-9. DOI: [10.1007/978-3-642-61485-9](https://doi.org/10.1007/978-3-642-61485-9) (cit. on p. 60).
- [86] Franz Schwabl. *Quantum mechanics*. OCLC: 185023213. Berlin; New York: Springer, 2007. ISBN: 978-3-540-71933-5. URL: <http://site.ebrary.com/id/10230332> (visited on 2018-10-24) (cit. on p. 61).
- [87] A. Bunse-Gerstner, R. Byers, and V. Mehrmann. “Numerical Methods for Simultaneous Diagonalization”. In: *SIAM Journal on Matrix Analysis and Applications* 14.4 (Oct. 1, 1993), pp. 927–949. ISSN: 0895-4798. DOI: [10.1137/0614062](https://doi.org/10.1137/0614062) (cit. on p. 62).
- [88] Terence Tao and Van Vu. “Random matrices have simple spectrum”. In: *arXiv:1412.1438 [math]* (Dec. 3, 2014). arXiv: [1412.1438](https://arxiv.org/abs/1412.1438). URL: <http://arxiv.org/abs/1412.1438> (visited on 2018-10-24) (cit. on p. 62).

Acknowledgments

I am very grateful to my thesis supervisors, Michael Sentef and Angel Rubio, for their support and guidance throughout my work on this project. Furthermore, I have greatly enjoyed working with the students and staff at MPSD and CFEL. In particular, I wish to thank Arunangshu Debnath, Henning Glave, Mona Kalthoff, Timo Lohrmann, Benedikt Mehmel, Salvador Ramírez-Acosta, Teresa Reinhard, Patricia Rihs, Michael Ruggenthaler, Christian Schäfer, Gabriel Topp, Riku Tuovinen, and Lukas Windgätter for their support and for helpful discussions. It has been a pleasure for me to be part of the MPSD Theory Department for the past year and I am looking forward to continue working in this environment for my PhD studies.

I have also benefited from discussions with Joel Yuen-Zhou on dark states in polariton systems and Thore Poßke on mathematical aspects of topological systems.

Computations have been performed on the EOS and Cobra clusters of the Max Planck Computing and Data Facility (MPCDF) in Garching.

Last, but not least, I wish to thank my family and friends for their support during my studies.

Eidesstattliche Erklärung

Ich versichere, dass ich die beigefügte schriftliche Masterarbeit selbstständig angefertigt und keine anderen als die angegebenen Hilfsmittel benutzt habe. Alle Stellen, die dem Wortlaut oder dem Sinn nach anderen Werken entnommen sind, habe ich in jedem einzelnen Fall unter genauer Angabe der Quelle deutlich als Entlehnung kenntlich gemacht. Dies gilt auch für alle Informationen, die dem Internet oder anderer elektronischer Datensammlungen entnommen wurden. Ich erkläre ferner, dass die von mir angefertigte Masterarbeit in gleicher oder ähnlicher Fassung noch nicht Bestandteil einer Studien- oder Prüfungsleistung im Rahmen meines Studiums war.

Die von mir eingereichte schriftliche Fassung entspricht jener auf dem elektronischen Speichermedium.

Ich bin nicht damit einverstanden, dass die Masterarbeit veröffentlicht wird.

Hamburg, 27. November 2018

Damian Hofmann